Displacement-dependent microstructural and petrophysical properties of deformation bands and gouges in poorly lithified sandstone deformed at shallow burial depth (Crotone Basin, Italy)

Displacement-dependent microstructural and petrophysical properties of deformation bands and gouges in poorly lithified sandstone deformed at shallow burial depth (Crotone Basin, Italy)

Mattia Pizzati*, Fabrizio Balsamo, Fabrizio Storti

NEXT, Natural and Experimental Tectonics Research Group, Department of Chemistry, Life Sciences, and Environmental Sustainability, University of Parma, 43124 Parma, Italy.

Corresponding author's E-mail address: mattia.pizzati@studenti.unipr.it

Corresponding author's phone number: +39 0521 905202

Keywords

Cataclastic deformation bands; sub-seismic deformation features; petrophysical properties; particulate flow-cataclasis; shallow-burial depth; high-porosity sandstone.

Highlights

- Fault zone characterized by sub-seismic scale deformation features.

- Permeability drops up to 3-4 orders of magnitude with respect to pristine sandstone.

- Particulate flow operates until porosity is > 5-6%, while below cataclasis settles.

- Deformation mechanism depends upon mineralogy of grains.

- Permeability and microstructures are strictly related to the total displacement.

Supplementary material

Detailed description of standard operating procedures adopted during grain size analysis and all the grain size distribution curves are provided with detailed permeability, grain size data and sampling sites along the studied fault zone. Moreover, inside the online supplementary file additional SEM photomicrographs, porosity, permeability data and grain shape analysis are provided with related statistical tests.

ABSTRACT

We present the results of meso-and micro-structural analyses performed on fault-related soft-sediment deformation structures affecting poorly lithified, high-porosity siliciclastic sediments in the Crotone Basin, Southern Italy. The investigated extensional fault zone has a total displacement of ~ 90 m and juxtaposes marine clayish sediments in the hanging wall against arkosic to lithic arkosic sandstone in the footwall. In the footwall damage zone, deformation is achieved by a network of conjugate deformation bands, whereas the foliated fault core hosts cm-thick gouges. Deformation bands and black gouges accommodated displacement between 0.2 to 20 cm. Microstructural observations and quantitative image analysis pointed out that particulate flow operated during the early stages of faulting, followed by cataclasis after significant porosity loss. Mineralogy of clasts controlled grain-scale deformation mechanism: following this, feldspar experienced extensive intragranular crushing, while quartz grains were deformed mainly by splitting and abrasion. Permeability of pristine sandstone spans from 5.4×10^4 to 1.4×10^5 mD, while inside deformation bands is reduced by 1-2 orders of magnitude, reaching 3-4 orders of magnitude within fault gouges. Permeability drop inside the fault zone is related to the accommodated displacement along each deformation structure, potentially leading to hydraulic compartmentalization of high-porosity sandstone reservoir.

1. Introduction

Fault zones in poorly lithified sediments and high-porosity rocks typically behave as barriers toward subsurface fluid flow, due to the development of deformation structures such as deformation bands and gouge layers in damage zones and fault cores, respectively (Antonellini and Aydin, 1994; Balsamo and Storti, 2010; Bense et al., 2013; Rotevatn et al., 2013; Ballas et al., 2015). Deformation bands can develop both as single structures or as clusters formed by tens to hundreds discrete elements, within which slip localizes along few discrete surfaces during progressive strain-hardening (Aydin and Johnson, 1978; Mair et al., 2000; Soliva et al., 2016; Fossen et al., 2017; Philit et al., 2018). Although strain-hardening is usually invoked as the main process leading to deformation band development, recent studies have pointed out that strain-softening may occur as well especially after reaching the yield point of the deformed material (Nicol et al., 2013). Deformation bands often show a limited lateral continuity with maximum length typically below 100 m, which is proportional to the accommodated displacement along each structure (Schultz and Fossen, 2002; Schultz et al., 2008). Fault gouges are usually found in high-strain domains and result by extreme grain size reduction and strain-localization processes (Engelder, 1974; Sibson, 1977; Balsamo and Storti, 2010). According to the classification of Sibson, (1977) the term gouge is used to identify incohesive fault rocks with less than 30% of visible clasts with respect to the fine-grained matrix. In the present contribution, we are referring to more specific fault rock types, namely black gouges, which are discrete elements showing extreme comminution and occur as isolated, or as an intricate network of deforming structures. Black gouges developing inside high-porosity sandstones were associated to a combination of grain size reduction and frictional heating produced during coseismic slip events related to shallow-depth (< 1 Km) earthquakes (Balsamo and Storti, 2011; Balsamo et al., 2014).

Petrophysical properties of deformation bands and fault gouges depend on several factors including lithological composition of host rock (Wilson et al., 2003; Exner and Grasemann, 2010; Cilona et al., 2012; Kristensen et al., 2013; Antonellini et al., 2014; Griffiths et al., 2016; Tavani et al., 2016; Cavailhes and Rotevatn, 2018), deformation mechanisms (Aydin, 1978; Aydin and Johnson, 1983; Bense et al., 2003; Rawling and Goodwin, 2003; Fossen et al., 2017), stress-strain conditions (Friedman and Logan, 1973; Olsson, 2000; Baud et al., 2012; Ballas et al., 2013; Robert et al., 2018) and microstructural features (Antonellini and Aydin, 1994; Main et al., 2000; Taylor and Pollard, 2000; Balsamo and Storti, 2011). In particular, different deformation mechanisms (cataclasis and granular-particulate flow) may cause a significant variability of permeability drops, from 1 up to 6 orders of magnitude with respect to the undeformed high-porosity protoliths (Ogilvie and Glover, 2001; Balsamo and Storti, 2010; Ballas et al., 2015; Fossen et al., 2017). Permeability diminishing in siliciclastic rocks is typically achieved through processes involving grain size reduction, sorting decrease and pore space collapse (Main et al., 2000; Balsamo and Storti, 2010; Kaproth et al., 2010). The recognition of fault structure and related deformation mechanisms is critical to assess the hydrological role of fault zones in sediments or high-porosity rocks hosting aquifers or hydrocarbon reservoirs (Bense et al., 2003; Parnell et al., 2004; Sternlof et al., 2006; Fossen and Bale, 2007; Kolyukhin et al., 2010). Further, burial depth during deformation is a key parameter that may influence the permeability drop associated with deformation band development (Ballas et al., 2015).

Despite the significant amount of work that has been done on the genesis and evolution of deformation bands (e.g., Antonellini et al., 1994; Cashman and Cashman, 2000; Mair et al., 2002a; Balsamo and Storti, 2010; Kaproth et al., 2010; Charalampidou et al., 2011; Fossen et al., 2017), basic scaling-laws such as the relationships between displacement and petrophysical properties are still a matter of debate (Torabi and Fossen, 2009; Ballas et al., 2012; Rotevatn et al., 2013, 2017). Previous studies mainly focused on the permeability ratio between faulted and undeformed rocks (Ballas et al., 2015; Fossen et al., 2017). With the present contribution, we attempt to provide additional details concerning the effect of total accommodated displacement on the microstructural features of deformation bands and gouges formed at shallow-burial conditions. Furthermore, the influence of microstructural-textural and petrophysical properties upon overall permeability was analyzed. For this purpose, we investigated in detail the microstructural and petrophysical properties of sub-seismic scale deformation structures occurring along the Rocca di Neto extensional fault zone affecting Pleistocene high-porosity sandstones in the Crotone Basin, Southern Italy. The footwall damage zone of the Rocca di Neto fault zone is characterized by widespread occurrence of deformation bands, both as single elements as well as clusters, and subsidiary faults with different amounts of displacement and grain size comminution. Black gouge layers are abundant in the foliated fault core, adjacent to the master slip zone. In this study, such sub-seismic scale structural elements were studied both at the meso and at the micro-scale. Petrophysical properties of deformed and undeformed sediments (permeability, grain size and porosity) were measured both by *in situ* and laboratory analyses. Complementary image analysis was used to quantify the grain shape and their preferred orientation. This multidisciplinary approach allowed us to constrain the evolution of deformation mechanism during faulting, which progressed from particulate flow to cataclasis, and to quantify the role of displacement in determining the petrophysical properties of faulted sandstones.

2. Geological setting and fault zone structure

The study area is located in the Crotone forearc basin, in Southern Italy (Fig. 1a), which developed as a consequence of subduction of the Adria plate below the European plate (e.g., Van Dijk et al., 2000; Zecchin et al., 2004; Reitz and Seeber, 2012). Basin infill began in Middle Miocene times, resulting in a stratigraphic succession as thick as 2500 m, overlying the metamorphic basement of the Sila Massif (Zecchin et al., 2004, 2012). Basin evolution includes five subsidence-uplift events during a dominant extensional and subtle transpressional tectonic history (Van Dijk and Scheepers, 1995; Van Dijk et al., 2000; Ferranti et al., 2009). Eventually, the onset of regional uplift since Middle Pleistocene times, led to the cessation of sedimentation and at the same time to the exhumation and surface exposure of the sedimentary succession (Knott and Turco, 1991; Antonioli et al., 2006; Zecchin et al., 2012; Massari and Prosser, 2013).

The present-day tectonic architecture of the onshore portion of the basin is defined by two major left-lateral shear zones bounding the basin to the NE and to the SW. A set of NE-SW-striking extensional fault zones accommodates displacement of several tens to hundreds meters in the centre of the basin (Van Dijk, 1994; Zecchin et al., 2004) (Fig. 1b). The Rocca di Neto fault zone belongs to the latter extensional fault system and affects Pleistocene sediments pertaining to the late-stage basin infill (Fig. 1c). In particular, the fault zone juxtaposes clayish sediments (Cutro Clay) in the hanging wall against silty sands, sandstones and conglomerates (Scandale Sandstone) in the footwall block (Zecchin et al., 2012) (Figs. 1c and 2a). The Cutro Clay was deposited in an offshore, shallow-marine environment, while the deposition of the Scandale Sandstone occurred in a shoreface setting where the majority of sediment supply was provided by a nearby river delta (Zecchin et al., 2012). Due to the unconsolidated nature of faulted sediments, the fault zone displays extensive occurrence of deformation features affecting high-porosity rocks (Balsamo and Storti, 2010; Pizzati et al., 2019), namely deformation bands and fault gouges. These structures are exclusively present in the footwall block of the fault, where high-porosity sandstones crop out. Conversely, the hanging wall block is almost completely covered by vegetation due to the presence of clayish sediments (Fig. 2a). Deformation bands are thin and well-localized tabular features that, when arranged in conjugate sets, typically have displacement between 1 and 5 cm. Deformation bands with displacement < 1 cm are found far from subsidiary faults and deformation band clusters. Fault-parallel deformation bands located closer to the master fault can display higher offsets, from 5 to 10 cm. Subsidiary faults accommodate larger amounts of displacement (> 15-20 cm) and are characterized by several cm-thick slip surfaces.

The overall structural architecture of the exposed footwall of the Rocca di Neto fault zone consists of four structural domains (Pizzati et al., 2019) (Fig. 2a, b): (1) a low-deformation zone, with widely spaced deformation bands and few subsidiary faults having low-displacement (Fig. 2b, c); (2) the damage zone, characterized by abundant conjugate deformation bands, together with subsidiary faults showing antithetic and synthetic shear sense with respect to the master fault (Fig. 2b, c); (3) the mixed zone, with a dense network of conjugate and high-strain fault-parallel deformation bands (Fig. 2b, c); (4) the fault core formed by foliated coarse to very fine sand cut by slip surfaces decorated by mm-to cm-thick black gouges (Fig. 2b, c). Although the majority of the total displacement is accommodated along the mixed zone and fault core, deformation bands and gouges significantly contribute to the offset partitioning along the entire fault zone.

Inside the low-deformation zone, and to lesser extent in the outer part of the footwall damage zone, deformation bands are arranged in conjugate sets and have offsets typically lower than ~ 1 cm (Fig. 3a). In the footwall damage zone, deformation bands are arranged in three sets; two of them form an inclined conjugate system (hereafter DB_1 and DB_2), while the third one ($DB_{//}$) is parallel to subsidiary faults (Fig. 3b). Within the mixed zone, deformation bands are organized in dense arrays, mostly trending parallel to subsidiary synthetic faults and to lesser extent arranged in conjugate arrays similar to the adjacent damage zone (Fig. 3c). Several 5-20 cm-thick clusters of fault-parallel deformation bands developed both in the damage zone and mixed zone, have cumulative offset typically exceeding 10 cm.

The studied cross-sectional exposure includes also the fault core, where most of the displacement is accommodated. This structural domain hosts several anastomosing slip surfaces decorated by black gouges (Fig. 2a, c) with thickness of ~ 1 cm, locally developing a gently folded pattern (Fig. 3d). Foliated sand encasing black gouges is highly deformed and tectonically compacted (Pizzati et al., 2019).

Inside the fault zone deformation bands and subsidiary faults often display evidence for selective cementation in the form of carbonate concretions made of calcite. Carbonate concretions develop tabular-to lens-shaped cemented bodies with thickness ranging from a few cm to 10-20 cm, paralleling the surface of the structural elements they encase (Fig. 3c, d). Cementation affects only deformation bands and subsidiary faults, while the host sandstone is completely non-cemented, except for rare, thin, bedding-parallel concretions displaying limited lateral continuity.

3. Analytical methods

3.1. Grain size analysis by laser diffraction

Sediment grain size was measured on 68 samples collected from different positions throughout the fault zone, according to the sediment type, position with respect to the master fault, and displacement (sampling sites are reported in Fig. 2a and Fig. A3 in the Supplementary Material). Samples were first dried at a constant temperature of 45°C for 48 hours, and then sieved with a 2000 μm mesh to remove impurities. Grain size analysis was performed with a Mastersizer 3000 (Malvern Instruments) laser diffraction particle size analyzer having an operating size range spanning from 0.01 to 3500 μm. In particular, we used the Hydro EV wet dispersion unit, with distilled water as dispersant fluid. Different analytical procedures were specifically developed for each sample type in order to minimize the alteration during the analysis (e.g. Storti and Balsamo, 2010). Details of tests and final grain size distributions are provided in the online Supplementary Material. Based on the grain size distribution curves, mean grain size, mode, span (sorting), and fractal dimension (D-value) were calculated. Span is defined as the width of the grain size distribution, while the D-value is calculated as the slope of the best-fit power-law distribution between grain size and cumulative frequency of particles per each grain size class in a log-log graph (Blenkinsop, 1991; Rawling and Goodwin, 2003; Balsamo and Storti, 2011).

3.2. In situ air permeability

A total of 652 *in situ* permeability measurements were performed across the fault zone using a portable Tiny Perm II air-permeameter (New England Research), which provides accurate data between 10^{-1} and 10^{5} mD, according to the methodology described by Balsamo et al. (2013). Permeability measurements were performed in the same sites where grain size samples were collected (see Fig. 2a and Figs. A2 and A3 in the online Supplementary Material), after careful brushing the target sediment to remove any alteration crust.

3.3. Image analysis technique

Fifty-five polished thin sections impregnated with blue-dyed resin were scanned at high resolution with a Nikon SuperCoolScan 5000 and studied with a Zeiss Axioplan 2 petrography microscope and a JEOL JSM 6400 scanning electron microscope (SEM), operating at 240 nA and 20 kV beam current. Two-dimensional porosity calculations were performed on 273 selected images acquired with the petrographic microscope at 12.5× magnification (thin section area 4747×3560 μm), both for the undeformed and faulted sandstone, using ImageJ open-source image analysis software (Schneider et al., 2012). A multi-scale image analysis technique was used to quantitatively describe particle shape. In particular, grains with equivalent diameter between 95 and 500 μm were investigated with 12.5× magnification, from 35 to 95 μm with 25× magnification (2352×1764 μm), from 25 to 35 μm with 50× magnification (1242×932 μm) and those between 10 and 25 μm with 100× magnification (614×461 μm). Particles finer than 10 μm were not taken into account because of their size below the resolution limit of the 100× optical microscope magnification. Particles with equivalent diameter greater than 500 μm are rare due to the medium-fine grain size of the analyzed samples. Grains were manually digitized at each magnification to prevent any bias and inaccuracy induced by the auto-tracing methods. Particle shape data were plotted against five grain size classes from 0 to 250 μm, with 50 μm bin size. Typically, more than 30 data were collected and averaged for each grain size class to grant statistical significance of the shape descriptors.

Three shape descriptors were used, namely aspect ratio, circularity and solidity. Aspect ratio (AR) is defined as:

$$AR = \frac{Major\ axis}{Minor\ axis} \quad (1)$$

where *Major axis* indicates the segment connecting the two farthest points along the perimeter of the grain, while *Minor axis* is the segment having as tips the nearest points on the perimeter. Values span from 1 (equant particle) to infinity (very elongated particle). Circularity (C) is given by:

$$C = \frac{4\pi A}{p^2} \quad (2)$$

where *A* is the total area of the grain and *p* is the perimeter. Circularity spans from 0 (extremely elongated and irregular shape) to 1 (perfect circle). Solidity (S) is defined as:

$$S = \frac{A}{A_{conv}} \quad (3)$$

where A_{conv} is the convex area delimited by the convex hull. Solidity varies from 0 (grain with extremely rough surface) to 1 (grain with very smooth surface).

Grain preferred orientation was also analyzed by measuring the angle between grain major axis and a horizontal reference plane. Half-rose diagrams were produced, using dotted lines to represent orientations of the investigated deformation structures in the thin sections.

4. Petrographic and microstructural characterization

4.1. Petrography of undeformed sandstone

The composition of the undeformed sandstone was constrained by modal analysis on 35 selected photomicrographs acquired at 12.5× magnification (thin section area 4747×3560 μm), via image analysis extracting the area percentage of the most recurrent mineralogical species. According to the results, 23 pristine sandstone samples lay in the lithic arkose field, while 12 of them plot in the arkose field in the Q-F-L ternary diagram of Folk (1974) (Fig. 4a). In particular, quartz percentage spans from 50.3 to 67.7%, while feldspar ranges from 19.6 to 36.9% and lithics from 5.3 to 18.2%. Lithics mainly include gneiss and granitic rock fragments, but sedimentary detrital grains also occur in the form of calcite grains and fossil shells. Other less frequent lithics are biotite mica, iron oxides-hydroxides, rare muscovite, chlorite and glauconite.

4.2. Microstructures

Deformed sandstone shows a variety of microstructures, according to the total displacement. In the low-deformation zone, deformation bands are tabular structures with a minimum thickness of 1-5 mm and sharp boundaries with the surrounding pristine sandstone (Fig. 4b). Grain size reduction is negligible and depositional fabric re-organization results in significant porosity loss. Deformation bands having few cm of displacement show grain size reduction, mainly produced by fragmentation of coarser feldspar grains and quartz abrasion (Fig. 4c). In particular, feldspar grains are deformed by several intragranular fractures, leading to the formation of tens of clasts, while quartz grains show mostly splitting and flaking of asperities (Fig. 5a, b). When displacement approaches or overcomes 10 cm, deformation bands are up to 5-6 mm-thick and display outer sectors made of comminute and crushed grains, and ~ 300 μm-thick cores where grain size reduction is more intense (Fig. 4d). The abundant dark brown matrix is dominantly composed of crushed feldspar and lithic grains, together with fine-grained quartz chips and to lesser extent fragments of detrital calcite. Locally, feldspar and quartz oversized survivor grains are present within the core of deformation bands and are cushioned by finer particles, which prevented their fracturing (Fig. 5c, d).

Black gouges have complex microstructural features, characterized by the presence of ultra-comminute 500-1000 μm-thick slip zones encased by less comminute sand volumes where subtle S-C structures are imparted by preferential orientation of mica flakes and coarse survivor grains (Fig. 4e). Fault cores of subsidiary faults show intense grain size comminution with several oversized survivor grains surrounded by a fine-grained matrix (Fig. 4f). Along deformation bands and gouges grain fracturing markedly occurs in their outer portion, whereas in the interior clasts are rarely affected by fractures (Fig. 6a). A gradient of comminution intensity is frequently observed in deformation band cores, resulting in the progressive increase of grain size from one boundary to the other (in Fig. 6b the left (footwall side) boundary of the deformation band is more comminute than the right side). High-displacement deformation bands sampled in the footwall damage zone commonly display a more pronounced grain size reduction on the footwall side. Conversely, deformation bands inside the fault core and mixed zone are characterized by asymmetric grain size reduction on the hanging wall side. Black gouges show the same gradient of grain size reduction as the one observed in deformation bands, but typically it is more intense along the hanging wall rather than on the footwall side (right side in Fig. 6c); thus these deformation elements display an asymmetric structure at the micro-scale.

5. Grain size data

Undeformed protoliths in the low-deformation zone are mainly composed of well-sorted, medium-to fine-grained sand with a mean size of 334 μm and, subordinately, medium-coarse sand with a mean size of 501 μm (Fig. 7a and table 1). Span values are very low for both sediment types (1.7 and 1.2, respectively; Fig. 7b). In the low-displacement zone, deformation bands have mean grain size of 236 μm, a mean span of 3.3 (Fig. 7a, b).

Moving to the footwall damage zone, the mean grain size of medium-fine sand layers composing the interband domain (i.e., the sand volume in between two adjacent deformation bands) decreases to 249 μm, whereas interband coarse sand has mean grain size of 614 μm (Fig. 7a), with mean span values of 1.9 and 3.1, respectively (Fig. 7b).

Conjugate deformation bands with different displacement magnitude inside the footwall damage zone display a range of grain size from 127 to 339 μm, while span varies from 4.6 to 8.1 (Fig. 7a, b).

Subsidiary faults and thick clusters of deformation bands have a mean grain size of 123 μm and a mean span of 5.8 (Fig. 7a, b).

Inside the footwall mixed zone, foliated sand is characterized by a mean grain size of 54 μm and a mean span of 9.2. Along the same structural domain, thin black gouges display mean grain size of 57 μm, with a mean span of 12.8 (Fig. 7a, b).

The fault core hosts foliated and stretched coarse sand pods characterized by a mean grain size of 428 μm and mean span of 4.3 (table 1). Foliated very fine sand displays a mean grain size of 84 μm, with mean span of 5.4. Eventually, black gouges in the fault core are characterized by mean grain size of 49 μm and a mean span of 11.2 (Fig. 7a, b). Details on granulometric curves of undeformed and deformed sediment samples are provided in the online Supplementary Material and in table 1.

Overall, low-displacement deformation bands induce an almost 2 times decrease of mean grain size, while medium-to high-displacement bands may reach mean grain size 3 times finer than the undeformed medium-fine sand. Black gouges and foliated very fine sand inside the fault core are characterized by mean grain size 7 and 5 times finer than the corresponding pristine medium-fine sand, respectively. Deformed sediment samples show a progressive increase in span, with the highest values characterizing deformation features inside the mixed zone and fault core (Fig. 7a, b).

While the comparison of samples in Figure 7 provides a summary of grain size data through the entire fault zone, accurate analysis of grain size variability induced by deformation is possible by evaluating granulometric curves of adjacent sample pairs as in Figure 8 (Storti et al., 2003). To this end, representative samples of deformation bands and gouges characterized by different displacement magnitudes were compared with the adjacent host sediments (undeformed in the low-deformation domain, and tectonically compacted foliated sand within mixed zone and fault core). In particular, a low-displacement deformation band collected inside the low-deformation zone is characterized by a mean grain size of 185 μm with a modal peak at 225 μm, while the undeformed medium-fine sand has a mean grain size of 280 μm and a modal peak at 320 μm (Fig. 8a). The shape and span of the grain size distribution curves are almost the same. Although similar, the D-value of the deformation band is slightly higher compared to the undeformed host sand (2.307 and 2.242, respectively) (Fig. 8b). The ratio between the number of faulted vs undeformed particles points out a relative increase of particles between the range from 0.4 to 240 μm in the deformation band and a decrease of coarse particles from 240 to 500 μm (Fig. 8c). The medium-displacement deformation band collected inside the footwall damage zone is characterized by a mean grain size of 155 μm, having a modal value of 225 μm, whereas the undeformed counterpart has a mean grain size of 248 μm with modal value of 200 μm (Fig. 8d). The D-value shows marked differences between the two samples, with the medium-displacement deformation band attesting at 2.634, while the adjacent interband domain has 2.3 (Fig. 8e). The deformed domain is characterized by an increase in fine particles in the range between 0.4 and 86 μm, with respect to the undeformed sample, while displays a decrease of coarse particles from 86 to 1630 μm (Fig. 8f). High-displacement deformation band in the footwall damage zone has a mean grain size of 95 μm having slightly pronounced trimodal distribution with relative maxima at 0.7, 30 and 230 μm (Fig. 8g). The interband domain is characterized by mean grain size of 248 μm with a modal value of 200 μm. The span of the grain size distributions is different with the deformation band showing a wider curve with respect to the undeformed control sample. D-value of the high-displacement deformation band is 2.769, much higher than the one characterizing the undeformed sand in the interband domain (2.3) (Fig. 8h). Below the 65 μm threshold, the high-displacement deformation bands shows a relative increase of particle number with respect to the undeformed host sand (Fig. 8i). Moving to the mixed zone, the fault core of a subsidiary fault displays mean grain size of 98 μm, with a trimodal distribution having relative maxima at 0.7, 29 and 160 μm. The adjacent sediment is formed by foliated sand with mean grain size of 72 μm, having similar distribution to the previous sample with relative maxima at 0.7, 26 and 153 μm (Fig. 8j). Span of the two granulometric distributions is almost the same. The fault core of the subsidiary fault has a D-value of 2.866 while for the foliated host sand is 2.776 (Fig. 8k). Inside the fault core of subsidiary fault the number of particles increases in the interval between 0.3 and 6.5 μm, and from 240 to 350 μm, while it decreases from 6.5 to 240 μm (Fig. 8l). Eventually, a black gouge sample inside the fault core is characterized by a mean grain size of 32 μm, with trimodal distribution having maxima at 0.6, 8 and 81 μm (Fig. 8m). The adjacent sediment is composed of foliated very fine sand with a mean grain size of 78 μm and a bimodal distribution with relative peaks at 0.7 and 62 μm. The D-value of black gouge is substantially higher than the one calculated for the foliated very fine sand (3.191 and 2.747, respectively) (Fig. 8n). Black gouge is characterized by an increase in the number of particles from 0.5 to 14.5 μm and from 516 to 586 μm, and by a relative decrease from 14.5 to 516 μm with respect to the foliated host sand (Fig. 8o).

6. Petrophysical properties

6.1. Permeability measurements

Along the footwall of the fault, *in situ* air-permeability shows a progressive decrease from the low-deformation zone toward the fault core (Fig. 7c). The highest permeability is recorded by medium-to fine-grained and coarse sandstone in the low-deformation domain, with mean values of 5.4×10^4 and 1.4×10^5 mD, respectively (Fig. 7c). Deformation bands with displacement < 1 cm, have almost half of the permeability shown by undeformed sandstone (3.1×10^4 mD). In the footwall damage zone, relatively undeformed medium-fine and coarse sandstones in the interband domain are characterized by mean permeability of 1.2×10^4 and 5.3×10^4 mD, respectively. Permeability in these interband sandstones shows a drop of at least half order of magnitude with respect to the undeformed sediments. Conjugate DB_1 and DB_2 sets inside the footwall damage zone have permeability spanning from 2.6×10^3 to 7.4×10^3 mD, thus causing a drop from 1 to 1.5 orders of magnitude (Fig. 7c). Fault core of subsidiary faults and thick clusters of deformation bands are characterized by a permeability drop up to 2 orders of magnitude (Fig. 7c). From the inner damage zone to the mixed zone, permeability shows an abrupt decrease in foliated sand layers and in thin black gouges (mean permeability of 193 and 201 mD, respectively) (Fig. 7c). Black gouges in fault core have mean permeability of 245 mD, with 7 mD as the lowest recorded value, thus featuring an overall permeability drop of 3 to 4 orders of magnitude with respect to the undeformed sandstone. In the same domain, foliated very fine sand and stretched very coarse sandstone recorded mean permeability of 496 and 4026 mD, respectively (Fig. 7c).

6.2. Two-dimensional porosity calculation

Primary porosity was calculated from acquired images neglecting any secondary porosity related to rare tensile micro-fractures and dissolution of fossil shells. Undeformed sandstone samples, from fine-to coarse-grained, have a mean 2-D porosity of 37.6% with a wide range of variation between 27.5 and 50.6% (Fig. 7d). Sediment volumes between deformation bands, both in the low-deformation and in the damage zone domains (interband domain), show a mean 2-D porosity of 29.7%. In the footwall damage zone, deformation bands with different displacement magnitude display a wide range of porosity values from 0.3 to 31.9% with a mean of 3.9% (Fig. 7d). Subsidiary faults and thick clusters of deformation bands inside the inner part of the damage zone are characterized by a mean porosity of 1.1%. In the footwall mixed zone, foliated sand volumes outside deformation bands have a mean porosity of 2.2%, while thin black gouges reach 1% (Fig. 7d). Eventually, foliated coarse sand pods in the fault core display a mean porosity of 2.9%, while foliated very fine sand reaches 0.8%. Black gouges encompassing the master fault are again characterized by very low porosity values below 1% (Fig. 7d).

At the micro-scale, porosity calculation performed along transects through deformation bands provides more details relative to porosity distribution (Fig. 9). In particular, a strand of low-displacement deformation bands has an almost symmetrical decrease of porosity (porosity decrement is almost the same on both sides of the deformation band) (Fig. 9a). On the contrary, a high-displacement deformation band has more pronounced asymmetry of porosity decrease from side to side (Fig. 9b). In this sample, porosity shows a more gradual diminishing from left to right, while on the right side the decrease is more abrupt at the sharp contact with undeformed sand. Porosity values reflect the different grain size distribution along the deformation band due to the development of a preferential slip surface. The vast majority of deformation bands tend to localize the shear along the hanging wall side, but also a few samples with localization along the footwall side were documented. Eventually, the black gouge has a marked asymmetric porosity diminishing approaching the preferential slip surface localized on the right side of the figure (Fig. 9c). These deformation features are formed by several preferential slip zones contributing to the major internal complexity with respect to deformation bands. However, also in black gouges a major preferential slip zone can be identified and corresponds to the sharp porosity contrast between undeformed and deformed sand (Fig. 9c). Differently to deformation bands, black gouges localize strain solely along their hanging wall side.

7. Grain shape data

7.1. Cumulative data

In Figure 10 are shown the grain shape descriptors (aspect ratio, circularity and solidity) versus grain size classes for deformation bands (low, medium and high-displacement), black gouges and subsidiary faults. All grain shape data are reported as ratio between faulted and undeformed particles, so that the following graphs show the relative increase-decrease of shape parameters in comparison with the reference sandstone. The undeformed reference sample used is a medium-to fine-grained sand belonging to the low-deformation zone (detailed shape data of the undeformed reference sample are reported in the online Supplementary Material Fig. A8). Overall, the aspect ratio of grains composing the deformed domains is lower than the reference undeformed sample throughout almost the entire investigated grain size interval. Thus, deformed grains tend to be more equant than undeformed ones (Fig. 10a). The lowest aspect ratio values are recorded in the grain size interval between 0 and 100 μm, while at coarser grain size they increase approaching the undeformed reference sand. Only in the 200-250 μm interval, two deformation band samples show aspect ratio values above the undeformed reference, featuring an increase of particle elongation. Circularity of deformed particles is higher than undeformed medium-fine sand, with only two mean values lying below the reference in the 200-250 μm range (Fig. 10b). Following this, deformed particles have more regular and circle-like shape than grains composing the undeformed control sample. The highest circularity values are recorded in the finest grain size interval (0-50 μm), with a progressive decrease at coarse grain size classes (Fig. 10b). Eventually, solidity of deformed domains is higher compared to the undeformed sand except for one deformation band sample in the 200-250 μm grain size class (Fig. 10c). According to this, faulted particles display a smoother outer surface, with less asperities than the reference sample. Highest solidity values are shown in the finest grain size range (0-50 μm), while they progressively diminish with increasing grain size (Fig. 10c).

More details are provided by the comparison of grain shape data of the representative five structural deformation features taken into account. In particular, the aspect ratio values show a progressive diminishing through the entire grain size range considering low, medium, high-displacement deformation bands and the black gouge. The difference between each dataset is more pronounced at finer grain size, while values converge in coarser grain size classes (Fig. 10a). The subsidiary fault displays aspect ratio between the low and medium-displacement deformation bands. Comparison of circularity between single structures points out low-displacement deformation band having the lowest values, while black gouge has the highest ones (Fig. 10b). Medium and high-displacement bands lay in between the previously mentioned structures, with the subsidiary fault covering the low-circularity interval partially overlapping with low-to-medium-displacement bands (Fig.

10b). As seen before for the aspect ratio, also differences in circularity are more evident in the finer grain size classes, while they are less emphasized in the coarser range. Eventually solidity between the five structural features displays trends similar to circularity. In particular, a progressive increase of particle smoothness from low-displacement deformation band to black gouge is observed, with medium-to-high-displacement bands lying in between (Fig. 10c). The subsidiary fault sample is characterized by values overlapping with low-and medium-displacement deformation bands. Differences between each dataset are more pronounced in the fine grain size range rather than in the coarse one (Fig. 10c). In summary, (i) aspect ratio of deformed particles is generally lower (more equant shape) than the undeformed sample; (ii) circularity of faulted grains is higher (more rounded shape) than undeformed ones; (iii) solidity is higher (smoother grains) in faulted domains; (iv) the difference of shape descriptors from deformed to undeformed domains is more evident with increasing displacement, except for the subsidiary fault, which seems not to follow this trend.

For statistical analysis of the entire grain shape dataset the reader is referred to the on-line Supplementary Material tables A2, A3 and A4.

7.2. Quartz, Feldspar, and Lithic grain shape data

Figure 11 displays the shape descriptors (aspect ratio, circularity and solidity) versus grain size classes for deformation bands (low, medium and high-displacement), black gouges and subsidiary faults, subdivided according to grain mineralogy (quartz, feldspar and lithic fragments). All grain shape data are reported as ratio between faulted and undeformed particles; the undeformed reference sample is the same medium-to fine-grained sand used in Figure 10 (detailed shape data of the undeformed reference are reported in the online Supplementary Material Fig. A10). As a general observation, aspect ratio of the three dominant mineralogical phases is below the undeformed sandstone adopted as reference.

Thus, quartz, feldspar and lithic deformed grains are more equant than the undeformed ones (Fig. 11a). Quartz grains have higher aspect ratio values than feldspar and lithics especially in the finer (0-100 μm) and coarser (150-200 μm) grain size ranges, while the difference is less evident from 100 to 150 μm (Fig. 11a). The circularity graph shows that almost all plotted mean data are above the reference sample except for the quartz data belonging to subsidiary fault in the 150-200 μm range. This suggests that all three mineralogical species are characterized by higher circularity values than the undeformed sand (Fig. 11b). Quartz has lower values compared to feldspar and lithics throughout the entire grain size range. Conversely, feldspar has the highest value in the 0-50 μm grain size class, while at coarser grain size is exceeded by lithic fragments (Fig. 11b). Solidity graph indicates an increase of grain smoothness for quartz, feldspar and lithics in the entire investigated grain size interval, except for the quartz data characterizing the subsidiary fault in the 150-200 μm interval (Fig. 11c). Similarly to trends identified for circularity, also solidity shows quartz having lower mean values compared to feldspar and lithics. Through the observation of trends from every deformation structures it stems that the decrease of aspect ratio for quartz, feldspar and lithics with respect to undeformed sand is more pronounced at finer grain size. Conversely, in the coarse size range aspect ratio diminishing is less marked (Fig. 11a). Increasing offset from low-displacement band to black gouge is reflected by an overall wider aspect ratio difference with the undeformed control sample and by a more evident difference between quartz, feldspar and lithics in the fine-grained interval. Despite having the highest displacement, the subsidiary fault has aspect ratio values similar to the low-displacement deformation band (Fig. 11a). Also for circularity the increase of displacement is reflected in a wider difference between undeformed and deformed domains and also between quartz, feldspar and lithics along the same deformation structure. This difference is particularly marked in the finer grain size classes (0-100 μm), while it becomes faint and less easily distinguishable in the coarser interval (Fig. 11b). As pointed out before for the aspect ratio, also circularity of subsidiary fault has values comparable to deformation bands with limited offset. Solidity suggests trends between the three mineralogical species very similar to what described for circularity, with a marked difference with respect to the undeformed sample in the fine grain size classes (0-100 μm) and less pronounced in coarse interval (100-200 μm) (Fig. 11c). Also in this case, the subsidiary fault shows relatively low solidity values comparable to low-displacement deformation bands.

To summarize, (i) quartz grains are generally the more elongated and angular particles; (ii) feldspar grains are less elongated and more rounded than quartz; (iii) lithic fragments have highly varying shape descriptors; (iv) grain shape differences between quartz, feldspar and lithics generally increase with increasing displacement of deformation structures and are more marked at finer grain size range. The statistical analysis of grain shape dataset is provided in tables A4-A13 in the online Supplementary Material.

8. Grain preferential orientation

Grain preferential orientation was performed by calculating the angle between grain major axis and a reference horizontal plane. Data presented are not differentiated according to the mineralogy of grains (quartz, feldspar and lithics), so that they report the bulk preferential orientation of deformed and undeformed sand.

Low-displacement deformation band displays a weak grain preferential alignment parallel to the band direction, as highlighted by the high angular deviation from the direction of the band (Fig. 12a). In medium-displacement deformation band, grains have a marked preferred orientation, both parallel and at 50-60° clockwise from the direction of deformation band (Fig. 12b). Grains in high-displacement deformation band are strongly aligned along the band direction and the most frequent angular classes fall within 40°

counter-clockwise and 10° clockwise direction to the reference deformation band plane (Fig. 12c). Grain preferential orientation in black gouge is well evident, with the majority of grain major axes falling within a 35° counter-clockwise angular fan from the gouge layer direction (Fig. 12d). Subsidiary fault has most of the grains preferentially oriented at 30-35° clockwise from the fault (Fig. 12e). Increasing displacement magnitude produces a more evident grain preferential orientation, with particles paralleling the direction of the deformation element.

9. Discussion

9.1. Deformation mechanisms (particulate flow followed by cataclasis)

In Figure 13, are summarized the main structural, microstructural and petrophysical properties of deformation features documented in the Rocca di Neto fault zone. The studied fault developed at very shallow-burial depth as indicated by stratigraphic constraints (Zecchin et al., 2012) and by the very weak compaction shown by the undeformed high-porosity sandstone, collectively suggesting a maximum burial depth below 400-500 m (Paxton et al., 2002). In this framework, deformation bands with displacement < 1 cm (Fig. 3a), characterized by grain re-organization and little grain size reduction, are interpreted to develop by particulate flow in highly porous sandstone (e.g., Rawling and Goodwin, 2003; Balsamo and Storti, 2010; Rodrigues and Alves da Silva, 2018) (Figs. 4b and 13a). Particulate flow does not obliterate the original texture of pristine sandstone, but rather operates a re-organization of fabric leading to a closer packing of grains and to porosity reduction, increasing contacts between particles (Antonellini et al., 1994; Kaproth et al., 2010; Soliva et al., 2013; Griffiths et al., 2016) (Figs. 7d and 13a). In low-displacement deformation bands within the low-deformation domain, the difference between the shape descriptors of deformed and undeformed domains is less pronounced compared to the other deformation structures (Fig. 10a, b, c). This line of evidence supports particulate flow as the main deformation mechanism, causing very limited grain fragmentation throughout all the investigated size classes. Moving toward the master fault, deformation bands in the footwall damage zone show a more severe reduction of grain size, even for bands with few cm of displacement (Fig. 4c, d). Grains are internally fractured, indicating that cataclasis was the main deformation mechanism (Engelder, 1974; Aydin and Johnson, 1978; Blenkinsop, 1991; Balsamo and Storti, 2010) (Figs. 5a, b and 13b, c). Grain breakage leads to a pronounced reduction of interparticle porosity (Fig. 7d), due to the presence of small grain fragments filling pores (Antonellini et al., 1994; Kaproth et al., 2010; Skurtveit et al., 2013; Torabi, 2014). The interpretation of a cataclastic deformation mechanism is also supported by the significant difference of the shape parameters of the three main mineralogical phases involved in the deformation, with quartz grains resulting more elongated and angular with respect to feldspar and lithic grains (Fig. 11a, b, c). The difference of the shape descriptors is related to the development of grain-scale fractures produced by cataclastic processes involving the high-porosity sandstone (grain crushing, translation and rotation) (Balsamo and Storti, 2011; Skurtveit et al., 2013). Cataclasis is even more severe in high-displacement deformation bands inside the mixed zone and fault core, leading to the formation of a thin core with strongly comminute grain size and an ultra fine-grained matrix (Figs. 4d and 13d). The strongest degree of cataclasis is found in black gouges and in the fault core of subsidiary faults, where strain-localization is testified by the occurrence of ultra-comminute layers (Engelder, 1974; Mair et al., 2002b; Balsamo et al., 2014) (Figs. 4e, f and 13e, f). Microstructural observations, in conjunction with grain size and porosity data, suggest that particulate flow was active for displacement < 1 cm, whereas cataclasis settled for displacement > 1 cm and after a porosity loss to 5-6%. As highlighted by other authors, porosity exerts a strong control upon the deformation mechanism affecting porous granular materials (Flodin et al., 2003; Shipton et al., 2005; Schultz et al., 2010).

In the investigated high-porosity sandstone, a porosity value of 5-6% can be assumed as the critical threshold to switch from particulate flow to cataclasis. Below this threshold, grains are forced to deform mostly via intragranular fracturing and then by abrasion during rolling (Fig. 5a, b).

The fragmentation of grains via cataclasis, promotes the development of more equant, smoother and regular shaped grains compared to the undeformed sandstone (Blenkinsop, 1991; Heilbronner and Keulen, 2006; Storti et al., 2007; Balsamo and Storti, 2011) (Fig. 11a, b, c). Grain shape data indicate that cataclasis acted selectively according to the mineralogy of grains. This is evident considering the systematically higher aspect ratio and lower circularity and solidity values shown by quartz with respect to feldspar, especially in the finer grain size range (Fig. 11). This difference in deformation mechanism can be linked to the presence of cleavages and twinning planes along the crystal structure of feldspar, acting as preferential breakage surfaces (Exner and Tschegg, 2012; Nicchio et al., 2018; Del Sole and Antonellini, 2019) (Figs. 5b and 14). The presence of the aforementioned reticular weaknesses, promotes the development of intragranular fractures during incipient cataclasis, leading to the formation of several equant small-sized clasts (Antonellini et al., 1994; Kaproth et al., 2010; Balsamo and Storti, 2011) (Fig. 14b, c). Quartz grains are less sensitive to the development of intragranular fractures due to the lack of twinning planes and to a higher hardness compared to feldspar. This results in deformation achieved mainly by grain splitting and abrasion of the asperities, and subordinately by intragranular fractures, forming highly elongated finer, and more equant smoothed coarse grains (cf. Balsamo and Storti, 2011) (Fig. 14d). Lithic fragments deform both via intragranular, trans-granular fracturing as well as by abrasion (Fig. 14b, c).

However, the deformation mechanism affecting lithics vary according to grain mineralogy (micas, gneiss-granitic fragments, bioclasts).

9.2. Displacement-dependent cataclasis

The deformation intensity in studied sub-seismic scale structures is related to the total amount of displacement accommodated by each deformation element. The investigated deforming structures display a different maturity of cataclastic fabric with increasing displacement (Figs. 4 and 6). In particular, in low-to medium-displacement deformation bands cataclasis is rather immature as testified by the slight decrease of mean grain size and sorting (Figs. 7a, b and 8a-f). High-displacement deformation bands and fault core of subsidiary faults accommodating higher offset are characterized by a more mature cataclastic fabric as indicated by the pronounced grain size reduction and widening of granulometric curves (i.e., sorting decrease) (Figs. 4d, f and 7a, b). Black gouges inside the fault core are interpreted as the products of extreme cataclasis caused by strain-localization, leading to the formation of thin, ultra-comminute layers (Fig. 4e). The increasing cataclastic intensity with displacement can be inferred also from the shape parameters of grains, in particular by evaluating the difference between quartz and feldspar (Fig. 11). Pronounced cataclasis is also responsible for the development of a weak foliation, imparted by the preferential alignment of grains parallel or at low-angle to the orientation of the deformation bands and gouges (Cladouhos, 1999; Cashman and Cashman, 2000) (Fig. 12). In summary, the higher is the accommodated displacement, the strongest is the foliation with major axis of grains paralleling the direction of the deformation element.

At the micro-scale, grain comminution is not uniform within the deformation band, but it is commonly more intense near one of the boundaries. This asymmetry of grain size comminution is caused by progressive localization of deformation on one side of the band or gouge (Fig. 6b, c). The greater is the displacement, the stronger is the grain size reduction and the asymmetry of comminution within the deformation band, up to the development of a 100-200 µm-thick slip surface (Figs. 4d). We suggest that the strain-localization on one side of the deformation bands could be caused by the kinematic stress field active in the vicinity of the master fault (Pizzati et al., 2019). This is further confirmed by the occurrence of microstructural asymmetry only inside deformation features close to the master fault, where the additional stress field was stronger.

Field observations indicate that deformation bands, subsidiary faults and gouges in the studied fault zone tend to increase their displacement approaching the master fault surface (Figs. 2 and 3). This is in accordance with the increase of the maturity of cataclastic fabric (Figs. 4 and 6), and also with the progressive increase of sorting-span and D-value with higher displacement magnitudes (Figs. 7 and 8). Inside the mixed zone and fault core, the presence of high-displacement structures (with offset exceeding bedding thickness) favored also the grain-scale mixing of layers with different grain size. Tectonic mixing is a common process in thinly-bedded siliciclastic successions (Heynekamp et al., 1999; Rawling and Goodwin, 2006; Balsamo and Storti, 2011). In the studied fault zone, tectonic mixing is testified by the anomalous coarser grain size in cores of subsidiary faults with respect to the surrounding foliated very fine sand (Fig. 8j-l). A further evidence is provided by the shape descriptor values that do not follow the increasing displacement trend identified by the other deforming structures. This would suggest a mixing of sediment volumes with different grain size concealing the real effect of the high-displacement magnitude (Figs. 10 and 11).

In the studied fault zone, we documented deformation features showing severe cataclasis even if the host sandstone was buried at very shallow depth (< 400-500 m) (Zecchin et al., 2012). Following this, although typically favored by significant overburden, we suggest that cataclastic processes in high-porosity sandstones, may occur not only in deep-burial settings (2-3 Km) (Ballas et al., 2015; Fossen et al., 2017), but also at shallower depth. Our data show that the onset of cataclasis depends mainly on the total displacement magnitude and upon the evolution of petrophysical-textural properties of the sandstone in the early stages of deformation. Following this, deep burial conditions are not strictly necessary for the onset of cataclasis in high-porosity arkosic to lithic arkosic sandstones.

9.3. Displacement-dependent petrophysical properties

The deformation mechanism previously described causes a strong deterioration of petrophysical properties of faulted sandstone, as underlined by the permeability drop characterizing the most deformed domains (exceeding four orders of magnitude diminishing) (Figs. 7c and 15). From cross-correlation graphs between permeability and petrophysical-textural properties it is possible to verify the role of each parameter in causing overall permeability decrement (Fig. 15). In particular, permeability shows a progressive decrease with increasing displacement from deformation bands to black gouges and subsidiary faults. Permeability vs 2-D porosity relationship describes a linear decreasing trend with increasing displacement (Fig. 15a). Conversely, permeability vs grain size is best fitted by a power-law function, with finer grain size (higher displacement) correlating with lowest permeability values (Fig. 15b). Permeability vs sorting-span is again fitted by a power-law distribution, but with negative exponent. Grain size distribution curves with high span (wide curves) are related with the lowest permeability values (Fig. 15c). Thus, a decrease of 2-D porosity and grain size and at the same time span increase (sorting decrease) due to cataclasis in response to incremental displacement, strongly affect the permeability drop of faulted sandstone. From the three graphs is evident the anomalous values reported for the subsidiary fault, not following the displacement relationship described by the other structural elements (Fig. 15a, b, c). This discrepancy can be interpreted as a further evidence for tectonic mixing affecting deformation features with displacement exceeding sedimentary bed thickness (Heynekamp et al., 1999; Rawling and Goodwin, 2006). This implies that porosity as well as grain size and span data are the results of deformation mechanism (cataclasis) and mixing of sediments with different textural and petrophysical properties.

The influence of grain shape (aspect ratio, circularity and solidity) in determining the permeability drop was also checked (Fig. 15d, e, f). Cumulative data indicate that lower permeability values are associated with slightly lower aspect ratio (equant grains) characterizing deformed particles (Fig. 15d). Deformed domains with lower permeability show also higher circularity (circle-shaped grains) (Fig. 15e). Significant permeability drop is associated with higher particle solidity (smoother grains) (Fig. 15f). Although shape descriptors of undeformed and deformed sandstone display different values, differences are not so pronounced. This can be translated in a minor role played by the development of more equant, regular and smoothed particles via cataclasis to the overall permeability decrease (Fig. 15d, e, f). Following this, from the shown datasets we interpret 2-D porosity, grain size and sorting-span as the main drivers for permeability drop occurring with increasing displacement.

9.4. Implications for fluid flow

The deformation mechanism previously described causes a deterioration of petrophysical properties of the faulted sandstone following the increase of displacement. Even deformation bands with low-displacement (< 1 cm), accommodated dominantly via particulate flow, may show a permeability drop of at least half an order of magnitude (Fig. 16a). Deformation bands with higher displacement (1 cm < d < 5 cm), developing an immature cataclastic fabric, may induce a permeability decrease up to 1.5 orders of magnitude (Fig. 16b). High-displacement bands (5 cm < d < 10 cm) feature an effective permeability drop from 2 to 3 orders of magnitude, due to the pronounced cataclastic fabric formed via intense fragmentation followed by abrasion of grains during rolling and translation (Fig. 16c). In these bands, strain-localization may occur along the boundary between band and undeformed sand thus leading to a gradient of porosity and permeability drop approaching the preferential slip surface (Figs. 9 and 16c). Mature cataclasis affecting the core of subsidiary faults (d > 20 cm) and gouges (d ~ 15 cm) causes a drop of mean permeability up to 4 orders of magnitude due to extreme grain size reduction and to the highest measured span of the granulometric curves (Fig. 16d). Therefore, early stage particulate flow followed by cataclasis affecting poorly lithified sandstone can reduce the effective permeability up to 4 orders of magnitude even with moderate displacement (10-20 cm). Following this, displacement is a key factor in controlling the permeability of sub-seismic deformation structures developed in high-porosity rocks, in conjunction with burial depth and stress-strain conditions (Ballas et al., 2012, 2015).

The studied deformation features are likely to have played a barrier role toward fluids orthogonal to the strike of the structural elements (Fig. 7). However, the real influence upon fluid flow has to be related to the lateral continuity and three-dimensional arrangement of deformation bands and gouges (Shipton et al., 2005; Sternlof et al., 2006; Kolyukhin et al., 2010; Ballas et al., 2015). Moreover, lateral variations concerning thickness of deformation bands can be a critical parameter in decreasing the sealing potential at the scale of the single band (Rotevatn et al., 2013, 2017).

The presence of deformed whitish sand within deformation bands, surrounded by orange-brown stained undeformed sandstone due to iron oxide precipitation, suggests an effective sealing behavior even for a few cm displacement (Fig. 3a). Even tough, the barrier-conduit role within deformed high-porosity sandstone is not straightforward as it is in the case of fully lithified rocks (Caine et al., 1996; Evans et al., 1997; Fisher et al., 2018). Whereas in lithified rocks the fault core acts as an effective barrier and the damage zone as a preferential conduit, in granular materials the sealing behavior may depend on the hydrological conditions (Sigda and Wilson, 2003; Wilson et al., 2003; Balsamo et al., 2012). In water-saturated conditions deformation bands and gouges display a barrier role, while in unsaturated ones, they may act as partial conduits due to high retention time of fluids within the deformed sediments (Sigda and Wilson, 2003). The Rocca di Neto fault zone has a present-day barrier role (as testified by *in situ* permeability measurement) (Fig. 7c), while during the early stages of deformation, the partial conduit behavior is witnessed by the presence of selective cementation along deformation bands and faults (Balsamo et al., 2012; Pizzati et al., 2019). This change in hydrological behavior is likely related to the different diagenetic environments and water-saturation conditions experienced by the fault during the deformation history and basin-scale tectonic exhumation occurred since Middle Pleistocene.

Our results could be useful to evaluate the possible compartmentalization of high-porosity sandstone reservoirs deformed at shallow-burial depth, through development of sub-seismic deformation structures (deformation bands and gouges). Such deformation features may represent major hydraulic discontinuities even after few cm of accommodated displacement.

10. Conclusions

We described the meso-scale structural features, microstructural characteristics and petrophysical properties of the extensional Rocca di Neto fault zone, deforming lithic arkosic to arkosic poorly lithified shoreface sandstones. Deformation occurred at shallow-burial conditions (< 400-500 m) and the pristine sandstone was characterized by high primary porosity. On the basis of our observations we came to the following main conclusions:

1- The deformation mechanisms responsible for the development of deformation bands are non-destructive particulate flow followed by cataclasis. Cataclasis becomes dominant after porosity decrease to 5-6%, and is more intense with increasing displacement eventually forming black gouges in the fault core, characterized by extreme grain size reduction, poor sorting and high D-value.

2- Cataclasis acts differently according to the mineralogy of the deformed grains: feldspar grains deform mainly by intragranular fractures leading to several equant sub-grains with circular and more regular shape, while quartz grains are less affected by intragranular fractures and deform by flaking of asperities producing more elongated chips. Thus, the resulting quartz clasts are more elongated, less circular and less smooth with respect to feldspar ones at finer grain size, while the difference is less pronounced at coarser grain size range.

3- The intensity of cataclasis is more pronounced along deformation bands, subsidiary faults and black gouges accommodating high offset. At the scale of the whole fault zone, deforming structures are characterized by an increasing displacement gradient approaching the master fault surface. In high-strain structural domains (mixed zone and fault core) cataclasis along high-displacement structures is accompanied by tectonic mixing of sediments having different grain size.

4- In deformation bands and gouges, the grain size is drastically reduced (7-8 times) with respect to the pristine sandstone, and permeability shows drops up to 3-4 orders of magnitude, in agreement with the total displacement accommodated along single structures. Permeability decreases as a function of displacement, coupled with grain size and porosity diminishing and span increase (sorting decrease). Conversely, evolution of grain shape played a minor role in determining the magnitude of permeability drop associated with deformed domains.

5- Cataclasis-related sub-seismic deformation structures (deformation bands and gouges) developing in high-porosity sandstones are capable of locally compartmentalize reservoirs deformed at shallow-burial depth. The occurrence of cataclastic processes at very shallow-burial conditions is related to major extent to the evolution of petrophysical and textural properties of deformed sandstone following increasing displacement magnitude.

Acknowledgements

The reviewers Eric Salomon and Conrad Childs are deeply acknowledged for the precise and thorough revisions of the early version of the manuscript. The Editor Cess Passchier is thanked for the careful editorial work.

The authors would like to thank Andrea Comelli for thin section preparation and Luca Barchi (University of Parma) for support during SEM image acquisition. Cristian Cavozzi (University of Parma) is thanked for technical support. Federica Pessina (University of Parma) is also acknowledged for assistance during field work on the Rocca di Neto fault zone and in the Crotone Basin. This work has benefited from the equipments and framework of the COMP-HUB Initiative, funded by the 'Departments of Excellence' program of the Italian Ministry for Education, University and Research (MIUR, 2018-2022).

Author contributions: Mattia Pizzati carried out field and laboratory work, data interpretation, and wrote the manuscript; Fabrizio Balsamo participated to field work and data interpretation, and critically revised the manuscript; Fabrizio Storti participated to data interpretation, and critically revised the manuscript.

References

Antonellini, M., Aydin, A., 1994. Effect of faulting on fluid flow in porous sandstones: petrophysical properties. American Association of Petroleum Geologists Bulletin 78, 355–377. https://doi.org/10.1306/8D2B1B60-171E-11D7-8645000102C1865D

Antonellini, M., Aydin, A., Pollard, D.D., 1994. Microstructure of deformation bands in porous sandstones at Arches National park, Utah. Journal of Structural Geology 16, 941–959.

Antonellini, M., Petracchini, L., Billi, A., Scrocca, D., 2014. First reported occurrence of deformation bands in a platform limestone, the Jurassic Calcare Massiccio Fm., northern Apennines, Italy. Tectonophysics 628, 85–104. https://doi.org/10.1016/j.tecto.2014.04.034

Antonioli, F., Ferranti, L., Lambeck, K., Kershaw, S., Verrubbi, V., Dai Pra, G., 2006. Late Pleistocene to Holocene record of changing uplift rates in southern Calabria and northeastern Sicily (southern Italy, Central Mediterranean Sea). Tectonophysics 422, 23–40. https://doi.org/10.1016/j.tecto.2006.05.003

Aydin, A., 1978. Small faults formed as deformation bands in sandstone. Pageoph 116, 913–930.

Aydin, A., Johnson, A.M., 1983. Analysis of faulting in porous sandstones. Journal of Structural Geology 5, 19–31. https://doi.org/10.1016/0191-8141(83)90004-4

Aydin, A., Johnson, A.M., 1978. Development of faults as zones of deformation bands and as slip surfaces in sandstone. Pageoph 116, 931–942.

Ballas, G., Fossen, H., Soliva, R., 2015. Factors controlling permeability of cataclastic deformation bands and faults in porous sandstone reservoirs. Journal of Structural Geology 76, 1–21. https://doi.org/10.1016/j.jsg.2015.03.013

Ballas, G., Soliva, R., Sizun, J., Fossen, H., Benedicto, A., 2013. Shear-enhanced compaction bands formed at shallow burial conditions; implications for fluid flow (Provence, France). Journal of Structural Geology 47, 3–15. https://doi.org/10.1016/j.jsg.2012.11.008

Ballas, G., Soliva, R., Sizun, J.P., Benedicto, A., Cavailhes, T., Raynaud, S., 2012. The importance of the degree of cataclasis in shear bands for fluid flow in porous sandstone Provence, France. AAPG Bulletin 96, 2167–2186. https://doi.org/10.1306/04051211097

Balsamo, F., Aldega, L., De Paola, N., Faoro, I., Storti, F., 2014. The signature and mechanics of earthquake ruptures along shallow creeping faults in poorly lithified sediments. Geology 42, 435–438. https://doi.org/10.1130/G35272.1

Balsamo, F., Bezerra, F.H.R., Vieira, M.M., Storti, F., 2013. Structural control on the formation of iron-oxide concretions and Liesegang bands in faulted, poorly lithified Cenozoic sandstones of the Paraìba Basin, Brazil. Bulletin of the Geological Society of America 125, 913–931. https://doi.org/10.1130/B30686.1

Balsamo, F., Storti, F., 2011. Size dependent comminution, tectonic mixing and sealing behavior of a “structurally oversimplified” fault zone in poorly lithified sands: Evidence for a coseismic rupture? Bulletin of the Geological Society of America 123, 651–668. https://doi.org/10.1130/B30099.1

Balsamo, F., Storti, F., 2010. Grain size and permeability evolution of soft-sediment extensional sub-seismic and seismic fault zones in high-porosity sediments from the Crotone basin, southern Apennines, Italy. Marine and Petroleum Geology 27, 822–837. https://doi.org/10.1016/j.marpetgeo.2009.10.016

Balsamo, F., Storti, F., Gröcke, D., 2012. Fault-related fluid flow history in shallow marine sediments from carbonate concretions, Crotone basin, south Italy. Journal of the Geological Society, London 169, 613–626. https://doi.org/10.1144/0016-76492011-109.

Baud, P., Meredith, P., Townend, E., 2012. Permeability evolution during triaxial compaction of an anisotropic porous sandstone. Journal of Geophysical Research: Solid Earth 117, 1–23. https://doi.org/10.1029/2012JB009176

Bense, V.F., Gleeson, T., Loveless, S.E., Bour, O., Scibek, J., 2013. Fault zone hydrogeology. Earth-Science Reviews 127, 171–192. https://doi.org/10.1016/j.earscirev.2013.09.008

Bense, V.F., Van den Berg, E.H., Van Balen, R.T., 2003. Deformation mechanisms and hydraulic properties of fault zones in unconsolidated sediments; the Roer Valley Rift System, The Netherlands. Hydrogeology Journal 11, 319–332. https://doi.org/10.1007/s10040-003-0262-8

Blenkinsop, T.G., 1991. Cataclasis and Processes of Particle Size Reduction. Pageoph 136, 59–86.

Caine, J.S., Evans, J.P., Forster, C.B., 1996. Fault zone architechture and permeability structure. Geology 24, 1025–1028. https://doi.org/10.1130/0091-7613(1996)024<1025

Cardozo, N., Allmendinger, R.W., 2013. Spherical projections with OXS Stereonet. Computers & Geosciences 51, 193–205. https://doi.org/doi:10.1016/j.cageo.2012.07.021.

Cashman, S., Cashman, K., 2000. Cataclasis and deformation-band formation in unconsolidated marine terrace sand, Humboldt County, California. Geology 28, 111–114. https://doi.org/10.1130/0091-7613(2000)28<111:CADFIU>2.0.CO;2

Cavailhes, T., Rotevatn, A., 2018. Deformation bands in volcaniclastic rocks – Insights from the Shihtiping tuffs, Coastal Range of Taiwan. Journal of Structural Geology 113, 155–175. https://doi.org/10.1016/j.jsg.2018.06.004

Charalampidou, E.M., Hall, S.A., Stanchits, S., Lewis, H., Viggiani, G., 2011. Characterization of shear and compaction bands in a porous sandstone deformed under triaxial compression. Tectonophysics 503, 8–17. https://doi.org/10.1016/j.tecto.2010.09.032

Cilona, A., Baud, P., Tondi, E., Agosta, F., Vinciguerra, S., Rustichelli, A., Spiers, C.J., 2012. Deformation bands in porous carbonate grainstones: Field and laboratory observations. Journal of Structural Geology 45, 137–157. https://doi.org/10.1016/j.jsg.2012.04.012

Cladouhos, T.T., 1999. Shape preferred orientations of survivor grains in fault gouge. Journal of Structural Geology 21, 419–436. https://doi.org/10.1016/S0191-8141(98)00123-0

Del Sole, L., Antonellini, M., 2019. Microstructural, petrophysical, and mechanical properties of compactive shear bands associated to calcite cement concretions in arkose sandstone. Journal of Structural Geology 126, 51–68. https://doi.org/10.1016/j.jsg.2019.05.007

Engelder, J.-T., 1974. Cataclasis and the generation of Fault Gouge. Geological Society of America Bulletin 85, 1515–1522. https://doi.org/10.1130/0016-7606(1974)85<1515:catgof>2.0.co;2

Evans, J.P., Forster, C.B., Goddard, J. V, 1997. Permeability of fault-related rocks, and implications for hydraulic structure of fault zones. Journal of Structural Geology 19, 1393–1404.

Exner, U., Grasemann, B., 2010. Deformation bands in gravels: displacement gradients and heterogeneous strain. Journal of the Geological Society 167, 905–913. https://doi.org/10.1144/0016-76492009-076

Exner, U., Tschegg, C., 2012. Preferential cataclastic grain size reduction of feldspar in deformation bands in poorly consolidated arkosic sands. Journal of Structural Geology 43, 63–72. https://doi.org/10.1016/j.jsg.2012.08.005

Ferranti, L., Santoro, E., Mazzella, M.E., Monaco, C., Morelli, D., 2009. Active transpression in the northern Calabria Apennines, southern Italy. Tectonophysics 476, 226–251. https://doi.org/10.1016/j.tecto.2008.11.010

Fisher, Q.J., Haneef, J., Grattoni, C.A., Allshorn, S., Lorinczi, P., 2018. Permeability of fault rocks in siliciclastic reservoirs: Recent advances. Marine and Petroleum Geology 91, 29–42. https://doi.org/10.1016/j.marpetgeo.2017.12.019

Flodin, E., Prasad, M., Aydin, A., 2003. Petrophysical constraints on deformation styles in Aztec sandstone, Southern Nevada, USA. Pure and Applied Geophysics 160, 1589–1610. https://doi.org/10.1007/s00024-003-2377-1

Folk, R.L., 1974. Petrology of sedimentary rocks, Hemphill Publishing Company, Austin, pp. 190. https://doi.org/10.1017/CBO9781107415324.004

Fossen, H., Bale, A., 2007. Deformation bands and their influence on fluid flow. AAPG Bulletin 91, 1685–1700. https://doi.org/10.1306/07300706146

Fossen, H., Soliva, R., Ballas, G., Trzaskos, B., Cavalcante, C., Schultz, R.A., 2017. A review of deformation bands in reservoir sandstones: geometries, mechanisms and distribution. Geological Society, London, Special Publications 459, 9–33. https://doi.org/10.1144/SP459.4

Friedman, M., Logan, J.M., 1973. Lüders’ bands in experimentally deformed sandstone and limestone. Bulletin of the Geological Society of America 84, 1465–1476. https://doi.org/10.1130/0016-7606(1973)84<1465:LBIEDS>2.0.CO;2

Griffiths, J., Faulkner, D.R., Edwards, A.P., Worden, R.H., 2016. Deformation band development as a function of intrinsic host-rock properties in Triassic Sherwood Sandstone. Geological Society, London, Special Publications 435. https://doi.org/10.1144/SP435.11

Heilbronner, R., Keulen, N., 2006. Grain size and grain shape analysis of fault rocks.

Tectonophysics 427, 199–216. https://doi.org/10.1016/j.tecto.2006.05.020

Heynekamp, M.R., Goodwin, L.B., Mozley, P.S., Haneberg, W.C., 1999. Controls on Fault-Zone Architecture in Poorly Lithified Sediment, Rio Grande Rift, New Mexico: Implications for Fault-Zone Permeability and Fluid Flow. Haneberg, W.C., Mozley, P.S., Moore, J.C., and Goodwin, L.B., Eds., Faults and Subsurface Fluid Flow in the Shallow Crust: Washington D.C., USA, Geophysical Monograph 113, American Geophysical Union. 27–49.

Kaproth, B.M., Cashman, S.M., Marone, C., 2010. Deformation band formation and strength evolution in unlithified sand: The role of grain breakage. Journal of Geophysical Research: Solid Earth 115, 1–11. https://doi.org/10.1029/2010JB007406

Knott, S.D., Turco, E., 1991. Late Cenozoic kinematics of the Calabrian Arc, southern Italy. Tectonics 10, 1164–1172. https://doi.org/10.1029/91TC01535

Kolyukhin, D., Schueller, S., Espedal, M.S., Fossen, H., 2010. Deformation band populations in fault damage zone-impact on fluid flow. Computational Geosciences 14, 231–248. https://doi.org/10.1007/s10596-009-9148-8

Kristensen, M.B., Childs, C., Olesen, N., Korstgård, J.A., 2013. The microstructure and internal architecture of shear bands in sand-clay sequences. Journal of Structural Geology 46, 129–141. https://doi.org/10.1016/j.jsg.2012.09.015

Main, I., Kwon, O., Ngwenya, B., Elphick, S., 2000. Fault sealing during deformation band growth in porous sandstone. Geology 28, 1131–1134.

Mair, K., Elphick, S., Main, I., 2002a. Influence of confining pressure on the mechanical and structural evolution of laboratory deformation bands. Geophysical Research Letters 29, 49-1-49–4. https://doi.org/10.1029/2001GL013964

Mair, K., Frye, K.M., Marone, C., 2002b. Influence of grain characteristics on the friction of granular shear zones. Journal of Geophysical Research: Solid Earth 107, 1–9. https://doi.org/10.1029/2001JB000516

Mair, K., Main, I., Elphick, S., 2000. Sequential growth of deformation bands in the laboratory. Journal of Structural Geology 22, 25–42. https://doi.org/10.1016/S0191-8141(99)00124-8

Massari, F., Prosser, G., 2013. Late Cenozoic tectono-stratigraphic sequences of the Crotone Basin: Insights on the geodynamic history of the Calabrian arc and Tyrrhenian Sea. Basin Research 25, 26–51. https://doi.org/10.1111/j.1365-2117.2012.00549.x

Nicchio, M.A., Nogueira, F.C.C., Balsamo, F., Souza, J.A.B., Carvalho, B.R.B.M., Bezerra, F.H.R., 2018. Development of cataclastic foliation in deformation bands in feldspar-rich conglomerates of the Rio do Peixe Basin, NE Brazil. Journal of Structural Geology 107, 132–141. https://doi.org/10.1016/j.jsg.2017.12.013

Nicol, A., Childs, C., Walsh, J.J., Schafer, K.W., 2013. A geometric model for the formation of deformation band clusters. Journal of Structural Geology 55, 21–33. https://doi.org/10.1016/j.jsg.2013.07.004

Ogilvie, S.R., Glover, P.W.J., 2001. The petrophysical properties of deformation bands in relation to their microstructure. Earth and Planetary Science Letters 193, 129–142. https://doi.org/10.1016/S0012-821X(01)00492-7

Olsson, W.A., 2000. Origin of Lüders' bands in deformed rock. Journal of Geophysical Research 105, 5931–5938. https://doi.org/10.3109/17453674.2010.492765

Parnell, J., Watt, G.R., Middleton, D., Kelly, J., Baron, M., 2004. Deformation Band Control on Hydrocarbon Migration. Journal of Sedimentary Research 74, 552–560. https://doi.org/10.1306/121703740552

Paxton, S.T., Szabo, J.O., Ajdukiewicz, J.M., Klimentidis, R.E., 2002. Construction of an intergranular volume compaction curve for evaluating and predicting compaction and porosity loss in rigid-grain sandstone reservoirs. AAPG Bulletin 86, 2047–2067. https://doi.org/10.1306/61eeddfa-173e-11d7-8645000102c1865d

Philit, S., Soliva, R., Castilla, R., Ballas, G., Taillefer, A., 2018. Clusters of cataclastic deformation bands in porous sandstones. Journal of Structural Geology 114, 235–250. https://doi.org/10.1016/j.jsg.2018.04.013

Pizzati, M., Balsamo, F., Storti, F., Iacumin, P., 2019. Physical and chemical strain-hardening during faulting in poorly lithified sandstone: The role of kinematic stress field and selective cementation. GSA Bulletin 1–18. https://doi.org/10.1130/b35296.1

Rawling, G.C., Goodwin, L.B., 2006. Structural record of the mechanical evolution of mixed zones in faulted poorly lithified sediments, Rio Grande rift, New Mexico, USA. Journal of Structural Geology 28, 1623–1639. https://doi.org/10.1016/j.jsg.2006.06.008

Rawling, G.C., Goodwin, L.B., 2003. Cataclasis and particulate flow in faulted, poorly lithified sediments. Journal of Structural Geology 25, 317–331. https://doi.org/10.1016/S0191-8141(02)00041-X

Reitz, M.A., Seeber, L., 2012. Arc-parallel strain in a short rollback-subduction system: The structural evolution of the Crotone basin (northeastern Calabria, southern Italy). Tectonics 31, 1–23. https://doi.org/10.1029/2011TC003031

Robert, R., Robion, P., Souloumiac, P., David, C., Saillet, E., 2018. Deformation bands, early markers of tectonic activity in front of a fold-and-thrust belt: Example from the Tremp-Graus basin, southern Pyrenees, Spain. Journal of Structural Geology 110, 65–85. https://doi.org/10.1016/j.jsg.2018.02.012

Rodrigues, R. de S., Alves da Silva, F.C., 2018. Deformation bands and associated structures in the Tucano Basin, NE Brazil: A multiscale analysis. Marine and Petroleum Geology 96, 202–213. https://doi.org/10.1016/j.marpetgeo.2018.05.035

Rotevatn, A., Fossmark, H.S., Bastesen, E., Thorsheim, E., Torabi, A., 2017. Do deformation bands matter for flow? Insights from permeability measurements and flow simulations in porous carbonate rocks. Petroleum Geoscience 23, 104–119. https://doi.org/10.1144/petgeo2016-038

Rotevatn, A., Sandve, T.H., Keilegavlen, E., Kolyukhin, D., Fossen, H., 2013. Deformation bands and their impact on fluid flow in sandstone reservoirs: The role of natural thickness variations. Geofluids 13, 359–371. https://doi.org/10.1111/gfl.12030

Schneider, C.A., Rasband, W.S., Eliceiri, K.W., 2012. NIH Image to ImageJ: 25 years of image analysis. Nature Methods 9, 671–675. https://doi.org/10.1038/nmeth.2089

Schultz, R.A., Fossen, H., 2002. Displacement-length scaling in three dimensions: The importance of aspect ratio and application to deformation bands. Journal of Structural Geology 24, 1389–1411. https://doi.org/10.1016/S0191-8141(01)00146-8

Schultz, R.A., Okubo, C.H., Fossen, H., 2010. Porosity and grain size controls on compaction band formation in Jurassic Navajo Sandstone. Geophysical Research Letters 37, 1–5. https://doi.org/10.1029/2010GL044909

Schultz, R.A., Soliva, R., Fossen, H., Okubo, C.H., Reeves, D.M., 2008. Dependence of displacement-length scaling relations for fractures and deformation bands on the volumetric changes across them. Journal of Structural Geology 30, 1405–1411. https://doi.org/10.1016/j.jsg.2008.08.001

Shipton, Z.K., Evans, J.P., Thompson, L.B., 2005. The geometry and thickness of deformation-band fault core and its influence on sealing characteristics of deformation-band fault zones. Aapg Memoir 85, 181–195. https://doi.org/10.1306/1033723M853135

Sibson, R.H., 1977. Fault rocks and fault mechanisms. Journal of the Geological Society of London 133, 191–213.

Sigda, J.M., Wilson, J.L., 2003. Are faults preferential flow paths through semiarid and arid vadose zones? Water Resources Research 39, 1–14. https://doi.org/10.1029/2002WR001406

Skurtveit, E., Torabi, A., Gabrielsen, R.H., Zoback, M.D., 2013. Experimental investigation of deformation mechanisms during shear-enhanced compaction in poorly lithified sandstone and sand. Journal of Geophysical Research: Solid Earth 118, 4083–4100. https://doi.org/10.1002/jgrb.50342

Soliva, R., Ballas, G., Fossen, H., Philit, S., 2016. Tectonic regime controls clustering of deformation bands in porous sandstone. Geology 44, 423–426. https://doi.org/10.1130/G37585.1

Soliva, R., Schultz, R.A., Ballas, G., Taboada, A., Wibberley, C., Saillet, E., Benedicto, A., 2013. A model of strain localization in porous sandstone as a function of tectonic setting, burial and material properties; new insight from Provence (southern France). Journal of Structural Geology 49, 50–63. https://doi.org/10.1016/j.jsg.2012.11.011

Sternlof, K.R., Karimi-Fard, M., Pollard, D.D., Durlofsky, L.J., 2006. Flow and transport effects of compaction bands in sandstone at scales relevant to aquifer and reservoir management. Water Resources Research 42, 1–16. https://doi.org/10.1029/2005WR004664

Storti, F., Balsamo, F., 2010. Particle size distributions by laser diffraction: sensitivity of granular matter strength to analytical operating procedures. Solid Earth 1, 25–48. https://doi.org/10.5194/se-1-25-2010

Storti, F., Balsamo, F., Salvini, F., 2007. Particle shape evolution in natural carbonate granular wear material. Terra Nova 19, 344–352. https://doi.org/10.1111/j.1365-3121.2007.00758.x

Storti, F., Billi, A., Salvini, F., 2003. Particle size distributions in natural carbonate fault rocks: Insights for non-self-similar cataclasis. Earth and Planetary Science Letters 206, 173–186. https://doi.org/10.1016/S0012-821X(02)01077-4

Tavani, S., Vitale, S., Grifa, C., Iannace, A., Parente, M., Mazzoli, S., 2016. Introducing dolomite seams: Hybrid compaction-solution bands in dolomitic limestones. Terra Nova 28, 195–201. https://doi.org/10.1111/ter.12210

Taylor, L.W., Pollard, D.D., 2000. Estimation of in situ permeability of deformation bands in porous sandstone, Valley of Fire, Nevada. Water Resources Research 36, 2595–2606.

Torabi, A., 2014. Cataclastic bands in immature and poorly lithified sandstone, examples from Corsica, France. Tectonophysics 630, 91–102. https://doi.org/10.1016/j.tecto.2014.05.014

Torabi, A., Fossen, H., 2009. Spatial variation of microstructure and petrophysical properties along deformation bands in reservoir sandstones. AAPG Bulletin 93, 919–938. https://doi.org/10.1306/03270908161

Van Dijk, J.P., 1994. Late Neogene kinematics of intra-arc oblique shear zones: The Petilia-Rizzuto Fault Zone (Calabrian Arc, Central Mediterranean). Tectonics 13, 1201–1230. https://doi.org/10.1029/93TC03551

Van Dijk, J.P., Bello, M., Brancaleoni, G.P., Cantarella, G., Costa, V., Frixa, A., Golfetto, F., Merlini, S., Riva, M., Torricelli, S., Toscano, C., Zerilli, A., 2000. A regional structural model for the northern sector of the Calabrian Arc (southern Italy). Tectonophysics 324, 267–320. https://doi.org/10.1016/S0040-1951(00)00139-6

Van Dijk, J.P., Scheepers, P.J.J., 1995. Neotectonic rotations in the Calabrian Arc; implications for a Pliocene-Recent geodynamic scenario for the Central Mediterranean. Earth Science Reviews 39, 207–246. https://doi.org/10.1016/0012-8252(95)00009-7

Wilson, J.E., Goodwin, L.B., Lewis, C.J., 2003. Deformation bands in nonwelded ignimbrites: Petrophysical controls on fault-zone deformation and evidence of preferential fluid flow. Geology 31, 837–840. https://doi.org/10.1130/G19667R.1

Zecchin, M., Caffau, M., Civile, D., Critelli, S., Di Stefano, A., Maniscalco, R., Muto, F., Sturiale, G., Roda, C., 2012. The Plio-Pleistocene evolution of the Crotone Basin (southern Italy): Interplay between sedimentation, tectonics and eustasy in the frame of Calabrian Arc migration. Earth-Science Reviews 115, 273–303. https://doi.org/10.1016/j.earscirev.2012.10.005

Zecchin, M., Massari, F., Mellere, D., Prosser, G., 2004. Anatomy and evolution of a Mediterranean-type fault bounded basin: The Lower Pliocene of the northern Crotone Basin (Southern Italy). Basin Research 16, 117–143. https://doi.org/10.1111/j.1365-2117.2004.00225.x

Zecchin, M., Massari, F., Mellere, D., Prosser, G., 2003. Architectural styles of prograding wedges in a tectonically active setting, Crotone Basin, Southern Italy. Journal of the Geological Society 160, 863–880. https://doi.org/10.1144/0016-764902-099

Figure captions

Fig. 1. (a) Geographic position of the Crotone Basin in the framework of the Southern Apennine orogenic belt and Calabrian Arc. The thinly dotted line marks the landward limit of the on-shore portion of the Crotone Basin. (b) Simplified geological map of the Crotone Basin with the position of the study area along the extensional fault system affecting the middle sector of the basin (modified after Zecchin et al., 2003). (c) Detailed geological cross-section of the study area reporting the position of the Rocca di Neto fault zone (redrawn after Balsamo et al., 2012). The trace of the cross-section is indicated by the black and white star in Fig. 1b. ATB, Apennine thrust belt; CA, Calabrian Arc; CAW, Calabrian accretionary wedge; CB, Crotone Basin.

Fig. 2. Architecture and structural data of the studied fault zone (adapted from Pizzati et al., 2019). (a) Detailed geological cross-section through the footwall of the Rocca di Neto fault, developing inside the Early Pleistocene Scandale poorly lithified sandstone. The hanging wall is almost completely covered by vegetation and debris and hosts the Middle Pleistocene Cutro Clay. The blue dots along the fault zone represent the 68 permeability and grain size sampling-measuring sites. Dotted rectangles report the exact position of the photographs shown in Fig. 3. (b) Cumulative structural data of faults and deformation bands also reporting the extensional slickenlines (Schmidt equal area, lower hemisphere projection). The three mean planes of the identified deformation band sets are calculated from the contour of poles to deformation bands. Stereonets were realized with Allmendinger's "*Stereonet 10.0 software*" (Cardozo and Allmendinger, 2013). (c) Sketch illustrating the most recurrent deformation structures along the studied fault zone. DB_1, synthetic high-angle deformation band; DB_2, antithetic low-angle deformation band; $DB_{//}$, fault-parallel deformation band; SF, subsidiary fault; MF, master fault; FMZ, footwall mixed

zone; FC, fault core; c.i., contouring interval; n, number of measured faults and deformation bands

Fig. 3. Outcrop details of the main deformation elements. (a) Low-displacement deformation band (d < 1 cm), inside the low-deformation domain. See the whitish color of deformed sandstone within the band contrasting with the marked orange-colored oxidation front abutting at the contact with the outer part of the band (black arrows). (b) Conjugate deformation bands characterizing the footwall damage zone of the fault, organized in two distinct sets, synthetic high-angle (DB_1) and antithetic low-angle (DB_2) with respect to the master fault. A third set is composed of deformation bands parallel to subsidiary faults ($DB_{//}$). See the coin in the top left corner of the image for scale. (c) High-strain deformation band surrounding a subsidiary fault hosted at the boundary between the footwall damage zone and the mixed zone. The fault is selectively cemented via precipitation of calcite cement (CC) (see the coin for scale). (d) Black gouges inside the fault core encased by mixed coarse and fine foliated sand (pencil for scale). DB_1, synthetic high-angle deformation band; DB_2, antithetic low-angle deformation band; $DB_{//}$, fault-parallel deformation band; CC, carbonate concretion.

Fig. 4. (a) Ternary Quartz-Feldspar-Lithics diagram showing the modal composition of the pristine sandstone, following the classification of Folk (1974). Sediment composition was measured on 35 different petrographic images evaluating the percentage of the dominant mineralogical phases. Plane-polarized photomicrographs of microstructural features of deformation bands and gouges. (b) Low-displacement fault-parallel deformation band within the low-deformation zone showing grain re-orientation and limited fragmentation. (c) Fault-parallel deformation band ($DB_{//}$) within the footwall damage zone displaying pronounced grain size reduction. Coarse grains are surrounded by a fine-grained light-brown matrix formed by highly comminute fragments. (d) High-displacement fault-parallel

deformation band close to the master fault, with a well developed ultra-comminute central core showing brownish matrix and an outer part with less pronounced grain size reduction. Tiny tensile fractures may develop both parallel and inclined to the band direction (white arrows). (e) Thin black gouge with severe comminution of grains in localized shear zone and S-C type structures imparted by the alignment of survivor grains and clay minerals. (f) Fault core of a subsidiary fault with cataclastic fabric, given by highly heterogeneous grain size distribution and poor sorting. DB, deformation band; Q, quartz; F, K-feldspar; L, lithic fragment.

Fig. 5. Detailed plane-polarized photomicrographs of the grain-scale deformation features. (a) Pervasive crushing of lithic fragments and feldspar grains by intragranular and trans-granular fractures, in the outer part of a low-displacement band. Porosity of this sample is still high due to the lack of fine-grained matrix produced after severe grain crushing following higher displacement magnitude. (b) Details of intragranular fractures affecting feldspar, developed along crystal twinning planes, and flaking of asperities characterizing quartz grains. Pores are partially filled by a fine-grained matrix formed by quartz chips and feldspar fragments. (c) Oversized survivor feldspar grain in a medium-displacement band. The brown matrix is composed of fine-grained quartz, feldspar and calcite flakes. (d) Survivor grains of quartz inside a high-displacement deformation band, are not affected by fracturing or flaking. Qz, quartz; K-f, K-feldspar; L, lithic fragment; P, pore space.

Fig. 6. Back-scattered SEM photomicrographs of deformation bands and gouges. (a) Medium-displacement deformation band with grains, especially feldspar, affected by intragranular fractures in its outer part (white arrows). Conversely, inside the deformation band itself grains rarely display fractures. (b) High-displacement deformation band close to the fault core, displaying a central core with pronounced grain size reduction, developing a slip surface on one side of the core. Grain size reduction has a decreasing gradient from

the slip surface toward the other side of the band. This sample was selectively cemented by calcite precipitation during progressive deformation. (c) Black gouge characterized by extreme comminution along the slip zone and by a gradient of grain size reduction moving away from it. Black gouge samples are often characterized by slip localization along the hanging wall side. Qz, quartz; K-f, K-feldspar; L, lithic fragment; P, pore space; C, calcite cement; M, biotite mica; SS, slip surface.

Fig. 7. Inter-quartile box-whisker plots of petrophysical properties of the most recurrent lithologies and deformation elements throughout the fault zone. (a) Mean grain size obtained from the analyses performed with the laser granulometer. (b) Sorting-span of the grain size distribution curves. (c) *In situ* air-permeability values measured with the Tiny Perm II permeameter. (d) Two-dimensional porosity calculation from image analysis of thin section photomicrographs. LDZ, low-deformation zone; FDZ, footwall damage zone; FMZ, footwall mixed zone; FC, fault core; DB_1, synthetic high-angle deformation band; DB_2, antithetic low-angle deformation band; n, number of measurements or analyses.

Fig. 8. Comparison of grain size distribution curves, D-value (fractal dimension) and ratio of faulted vs undeformed particles between sample pairs representative of the most recurrent deformation features. Sample pairs were selected to directly compare deformed structures with the surrounding host sediments. D-value provides details concerning the cumulative particle number, indicating the number of fine vs coarse grains through a factor describing the slope of the power-law function fitting data distribution. Ratio of particle number between faulted and undeformed domains is useful to evaluate the relative increase or decrease of particles in a specific grain size range. Red color is used to distinguish deformed domains, while undeformed ones are reported in blue. (a, b, c) Low-displacement deformation band vs undeformed medium-fine sand inside the low-deformation zone. (d, e, f) Medium-displacement deformation band vs undeformed

medium-fine sand inside the footwall damage zone. (g, h, i) High-displacement deformation band vs undeformed medium-fine sand inside the footwall damage zone. (j, k, l) Fault core of subsidiary fault vs foliated very fine sand inside the footwall mixed zone. (m, n, o) Black gouge vs foliated very fine sand inside the fault core; GSD, grain size distribution; DB, deformation band; Φ, mean grain size; d, displacement.

Fig. 9. Plane-polarized photo-mosaics reporting the porosity variation across low-displacement band (a), medium-displacement band (b) and black gouge (c). Two-dimensional porosity is reported on profile crossing the entire length of the structural element as mean percentage calculated from the areas delimited by white dotted lines throughout the deformation structures.

Fig. 10. Grain shape analysis performed on cumulative data of the most representative deformation features: low, medium, high-displacement deformation bands, fault core of subsidiary fault and black gouge. Grains are described using three shape descriptors, aspect ratio (a), circularity (b) and solidity (c). Symbols represent mean values of the shape parameters plotted as ratio between the faulted and undeformed samples, to ease the recognition of differences and similarities between the five datasets. All data are subdivided in five distinct grain size classes, 50 μm each. Complete datasets are provided in the online Supplementary material Figs. A7 and A8, together with data regarding the undeformed medium-fine sand adopted as reference and statistical analysis. d, displacement; n, number of grains traced and analyzed via image analysis.

Fig. 11. Grain shape analysis performed on the three most recurred minerals (quartz, feldspar and lithic fragments) in low, medium, high-displacement deformation bands, fault core of subsidiary fault and black gouge. Grains are described using three shape descriptors, aspect ratio (a), circularity (b) and solidity (c). Symbols represent mean values

of the shape parameters plotted as ratio between the faulted and undeformed samples, to ease the recognition of differences and similarities between the five datasets. All data are subdivided in four distinct grain size classes, 50 μm each; the coarser grain size class from 200 to 250 μm was omitted because of the limited number of data unable to provide statistical robustness. Complete datasets are provided in the online Supplementary material Figs. A9 and A10, together with data regarding the undeformed medium-fine sand adopted as reference and statistical analysis. Qz, quartz; K-f, feldspar; L, lithic fragment; d, displacement; n, number of grains traced and analyzed via image analysis.

Fig. 12. Half-rose plots of the preferential orientation of grains according to the angle between the major axis and a horizontal reference plane. Undeformed control samples are on the left side (green diagrams), while deformed counterparts are on the right side of the figure (red diagrams). Preferential orientation for low-displacement (a), medium-displacement (b), high-displacement deformation band (c), black gouge (d) and subsidiary fault (e). Black dotted lines indicate the orientation of the deformation band, gouge or fault on thin section. d, displacement; n, number of grains.

Fig. 13. Microstructural features according to the identified deformation mechanism. (a) Inside the low-deformation zone and the outer damage zone, deformation bands accommodated small-scale displacement (typically < 5 cm). Along these structures deformation is mainly achieved via particulate flow with fabric re-organization and negligible grain fragmentation. This causes a decrease of porosity from 37% of the pristine sandstone to 5-7% within deformation bands. (b) In the outer footwall damage zone, higher displacement along deformation bands forced grains, especially feldspar, to break along crystal weaknesses such as twinning planes. Quartz is less affected by fragmentation via intragranular fracturing and deforms mainly by flaking and chipping of the asperities along the outer surface. (c) Inside the footwall damage zone, fault-parallel

deformation bands with displacement above 5 cm, are characterized by an immature cataclastic fabric, with grain size reduction and sorting diminishing. (d) High-displacement deformation bands may develop an inner core with severe grain size reduction, leading to the formation of a brownish matrix composed of crushed feldspar and calcite grains. To the outer part of the band grain size reduction is less pronounced. Eventually, within the mixed zone and fault core the most deformed end-members are located, with subsidiary faults (e) displaying an asymmetric structure with a slip surface and a decreasing gradient of grain size reduction moving away from it. Within the fault core, black gouges (f) display extreme grain crushing leading to the formation of ultra-comminute thin layers, encased by less deformed sand arranged in S-C arrays. The deformation mechanism described above is able to reduce the permeability up to 3.5-4 orders of magnitude with respect to the pristine high-porosity sandstone. K_{av}, average permeability; SS, slip surface; d, displacement.

Fig. 14. Grain-scale deformation mechanism. (a) Undeformed high-porosity sand. (b) Early deformation with compaction leading to intragranular crushing of feldspar and flaking of coarser quartz grains. Lithic fragments are affected by trans-granular as well as intragranular fractures. (c) With progressive deformation, crushing of feldspar produces sub-equant particles, while flakes of quartz grains display highly elongated shape with angular borders. (d) In the final stage of deformation, cataclasis forms angular fine-grained quartz flakes and equant-smooth fine-grained feldspar clasts. The oversized-survivor quartz and feldspar clasts are more equant and display smooth shape. Qz, quartz; K-f, feldspar; L, lithic grain; P, pore space.

Fig. 15. Relationships between permeability ratio of faulted and undeformed sediments with petrophysical properties and shape descriptors. (a) Permeability ratio vs 2-D porosity calculated on thin section. (b) Permeability ratio vs mean grain size measured by laser

diffraction. (c) Permeability ratio vs mean sorting-span gained from laser diffraction analysis. (d) Permeability ratio vs grain aspect ratio from cumulative data. (e) Permeability ratio vs grain circularity from cumulative data. (f) Permeability ratio vs grain solidity from cumulative data. The reference permeability was assumed as a mean of all permeability measurements on the undeformed sandstone outside the fault zone. Error bars represent the standard deviation associated with datasets. d, displacement; n, number of measurements, analysis and grains traced on thin section.

Fig. 16. Evolutionary model of deforming structures from low-offset deformation bands to faults. (a) Particulate flow affecting low-displacement deformation bands causes a weak grain size reduction and a closer packing of grains, leading to mean porosity of 5-6%. The reduction of porosity features a decrease of permeability of less than one order of magnitude. (b) In medium-displacement deformation bands the onset of fragmentation and rolling of grains results in an immature cataclastic fabric, responsible for the reduction of grain size and sorting. Porosity is further reduced (2-3%) as well as permeability (1.5 orders of magnitude less than undeformed sand). (c) High-displacement deformation bands are affected by pronounced cataclasis and strain-localization processes inducing an asymmetrical drop of porosity (~ 1%) and permeability (3 orders of magnitude less than the undeformed sandstone). (d) Eventually, along subsidiary faults with offset > 20 cm, cataclasis is extreme and severe grain size reduction leads to low values of porosity (< 1%) and to a permeability contrast up to 4 orders of magnitude with respect to the pristine sandstone. K_{fault}, average permeability of faulted sandstone; K_{und}, average permeability of pristine sandstone; d, displacement.

Table 1. Structural position, deforming element, distance from the master fault, mean diameter, mode, sorting-span (with associated standard deviation), D-value and R^2 of the analyzed grain size samples. LDZ, low-deformation zone; FDZ, footwall damage zone;

FMZ, footwall mixed zone; FC, fault core; MF, master fault; DB_1, synthetic high-angle deformation band; DB_2, antithetic low-angle deformation band.

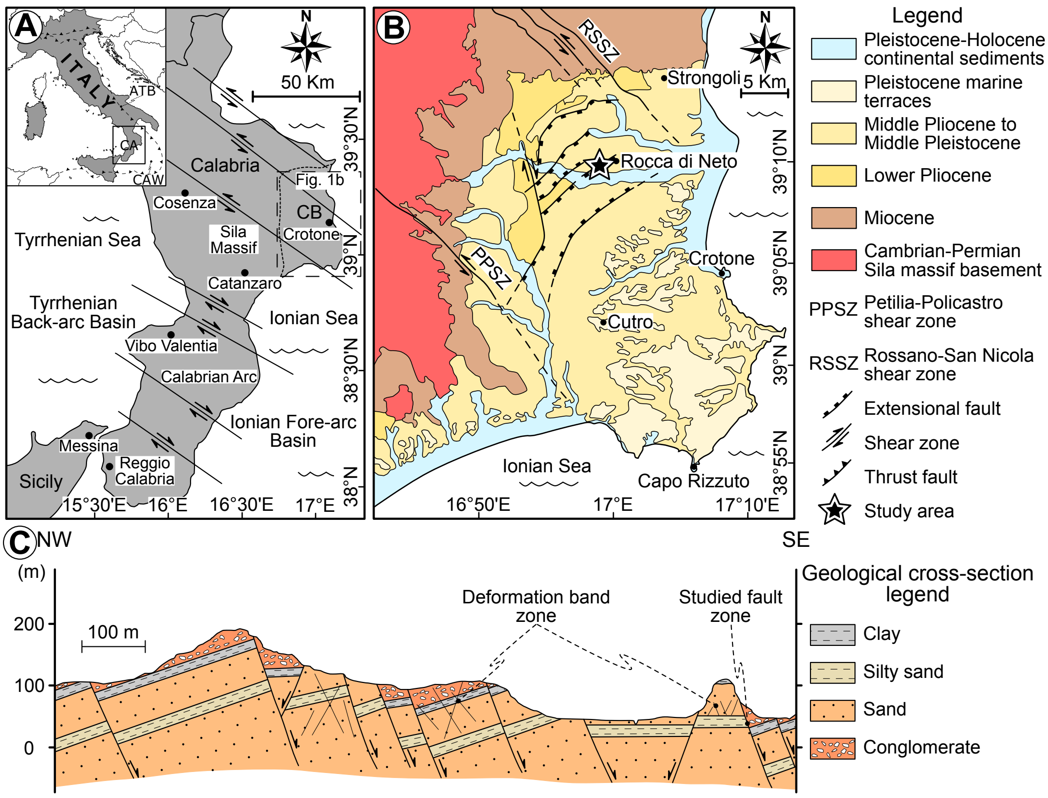

A
ITALY
ATB
CA
CAW
N
50 Km
Calabria
Fig. 1b
Cosenza
CB
Crotone
Sila Massif
Tyrrhenian Sea
Catanzaro
Tyrrhenian Back-arc Basin
Ionian Sea
Vibo Valentia
Calabrian Arc
Ionian Fore-arc Basin
Messina
Reggio Calabria
Sicily
15°30'E
16°E
16°30'E
17°E
39°30'N
39°N
38°30'N
38°N
B
RSSZ
Strongoli
5 Km
Rocca di Neto
PPSZ
Crotone
Cutro
Ionian Sea
Capo Rizzuto
16°50'E
17°E
17°10'E
39°10'N
39°05'N
39°N
38°55'N
Legend
Pleistocene-Holocene continental sediments
Pleistocene marine terraces
Middle Pliocene to Middle Pleistocene
Lower Pliocene
Miocene
Cambrian-Permian Sila massif basement
PPSZ Petilia-Policastro shear zone
RSSZ Rossano-San Nicola shear zone
Extensional fault
Shear zone
Thrust fault
Study area
C
NW
SE
(m)
200
100
0
100 m
Deformation band zone
Studied fault zone
Geological cross-section legend
Clay
Silty sand
Sand
Conglomerate

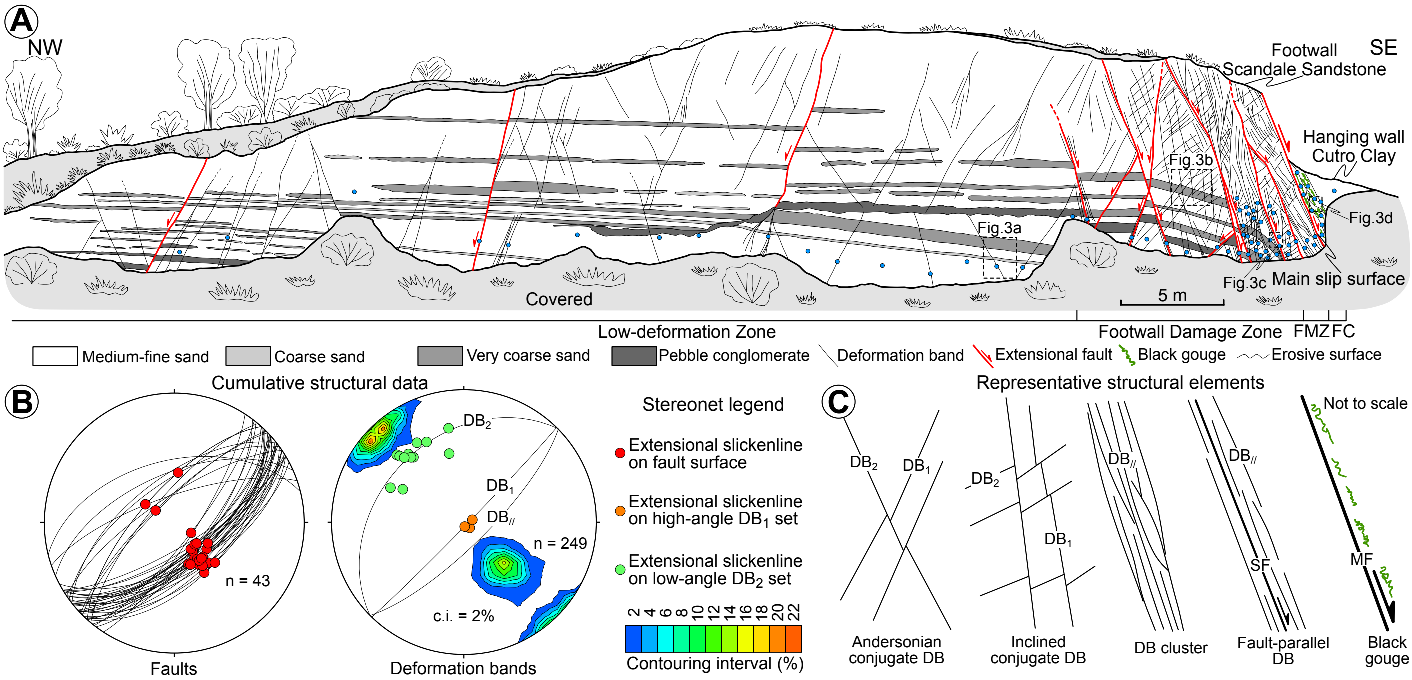
A
NW
SE
Footwall
Scandale Sandstone
Hanging wall
Cutro Clay
Fig.3b
Fig.3a
Fig.3d
Fig.3c
Main slip surface
Covered
5 m
Low-deformation Zone
Footwall Damage Zone
FMZ
FC
Medium-fine sand
Coarse sand
Very coarse sand
Pebble conglomerate
Deformation band
Extensional fault
Black gouge
Erosive surface
B
Cumulative structural data
n = 43
Faults
DB2
DB1
DB//
n = 249
c.i. = 2%
Deformation bands
Stereonet legend
Extensional slickenline on fault surface
Extensional slickenline on high-angle DB1 set
Extensional slickenline on low-angle DB2 set
2 4 6 8 10 12 14 16 18 20 22
Contouring interval (%)
C
Representative structural elements
Not to scale
DB2
DB1
Andersonian conjugate DB
DB2
DB1
Inclined conjugate DB
DB//
DB cluster
DB//
SF
Fault-parallel DB
MF
Black gouge

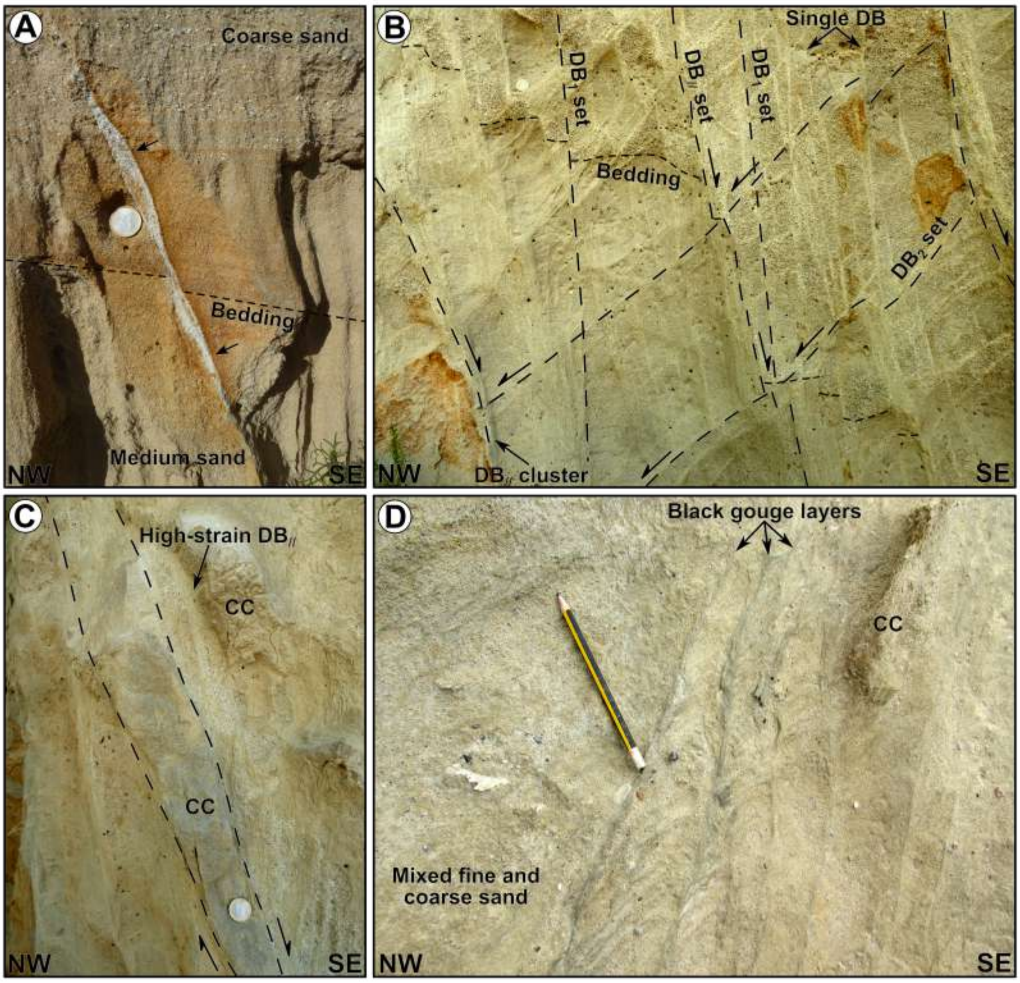
A
Coarse sand
Bedding
Medium sand
NW
SE
B
Single DB
DB_1 set
$DB_{//}$ set
DB_1 set
Bedding
DB_2 set
$DB_{//}$ cluster
NW
SE
C
High-strain $DB_{//}$
CC
CC
NW
SE
D
Black gouge layers
CC
Mixed fine and coarse sand
NW
SE

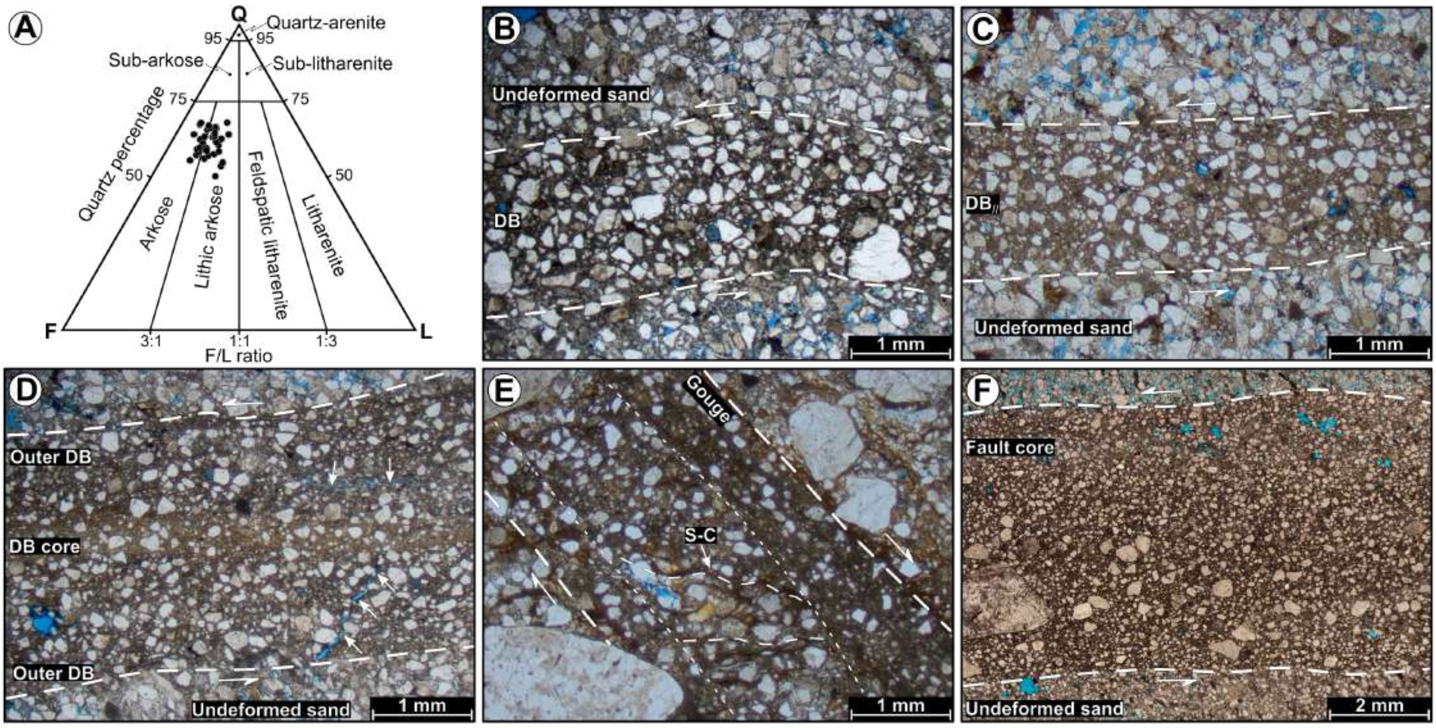

A
Q
Quartz-arenite
95
95
Sub-arkose
Sub-litharenite
75
75
Quartz percentage
50
50
Arkose
Lithic arkose
Feldspatic litharenite
Litharenite
F
L
3:1
1:1
1:3
F/L ratio
B
Undeformed sand
DB
1 mm
C
DB//
Undeformed sand
1 mm
D
Outer DB
DB core
Outer DB
Undeformed sand
1 mm
E
Gouge
S-C
1 mm
F
Fault core
Undeformed sand
2 mm

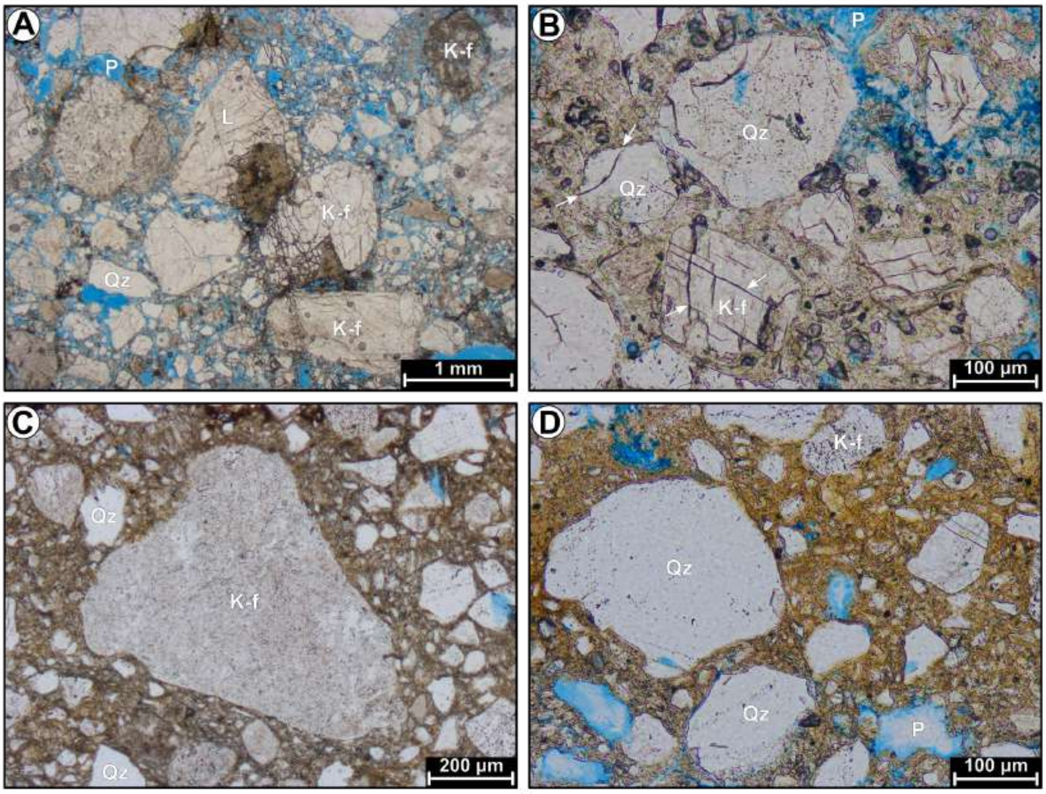
A
P
L
K-f
K-f
Qz
K-f
1 mm
B
P
Qz
Qz
K-f
100 µm
C
Qz
K-f
Qz
200 µm
D
K-f
Qz
Qz
P
100 µm

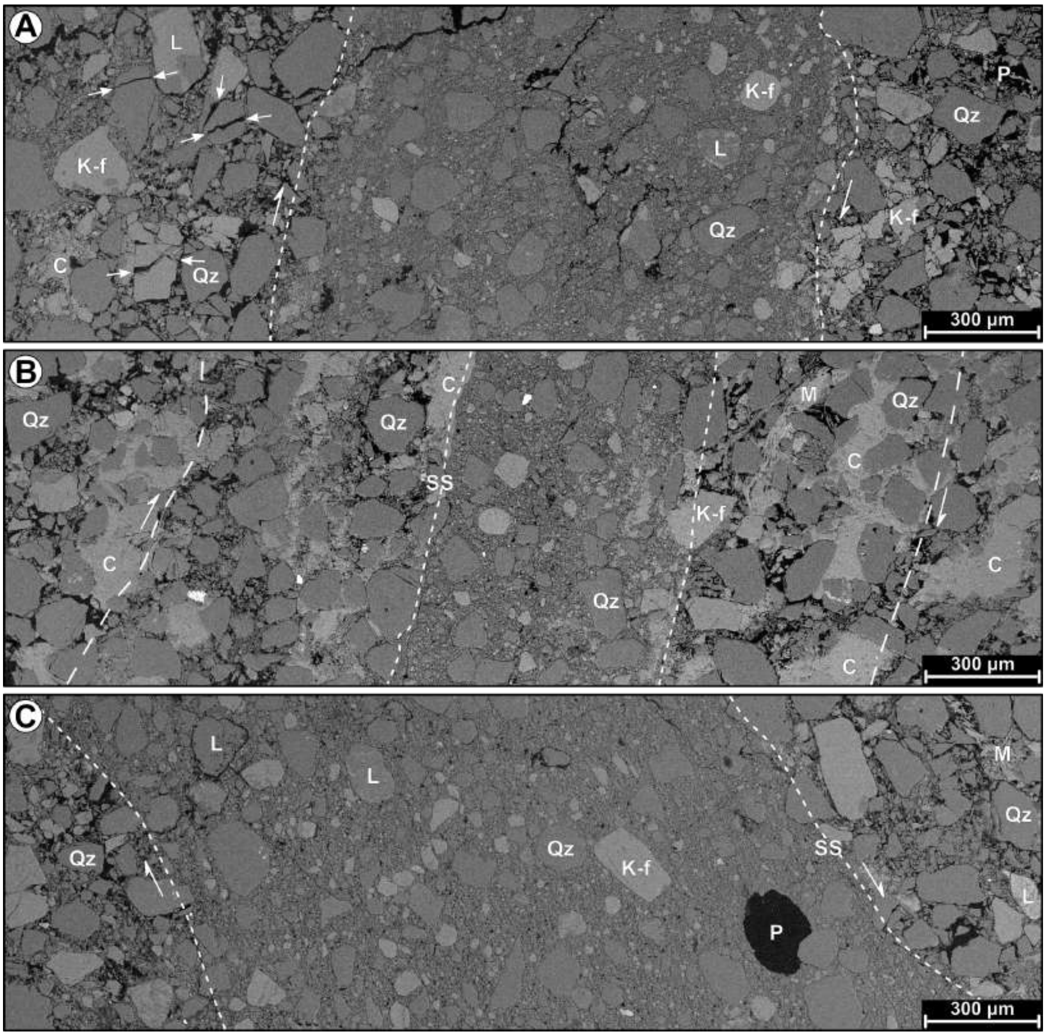

A
L
K-f
C
Qz
P
300 μm
B
Qz
C
SS
K-f
M
300 μm
C
L
Qz
K-f
P
SS
M
300 μm

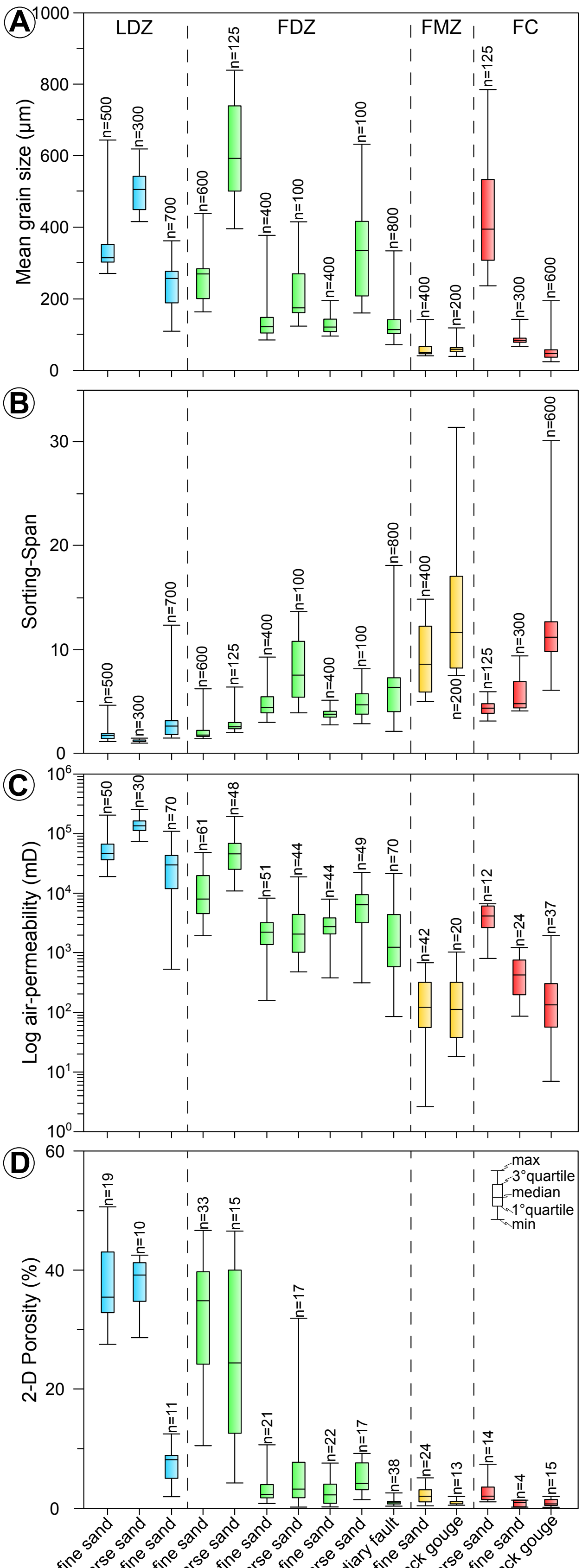
A
B
C
D
LDZ
FDZ
FMZ
FC
Mean grain size (μm)
Sorting-Span
Log air-permeability (mD)
2-D Porosity (%)
max
3°quartile
median
1°quartile
min
Medium-fine sand
Medium-coarse sand
DB medium-fine sand
Medium-fine sand
Medium-coarse sand
DB₁ medium-fine sand
DB₁ coarse sand
DB₂ medium-fine sand
DB₂ coarse sand
Subsidiary fault
Foliated very fine sand
Black gouge
Foliated coarse sand
Foliated very fine sand
Black gouge

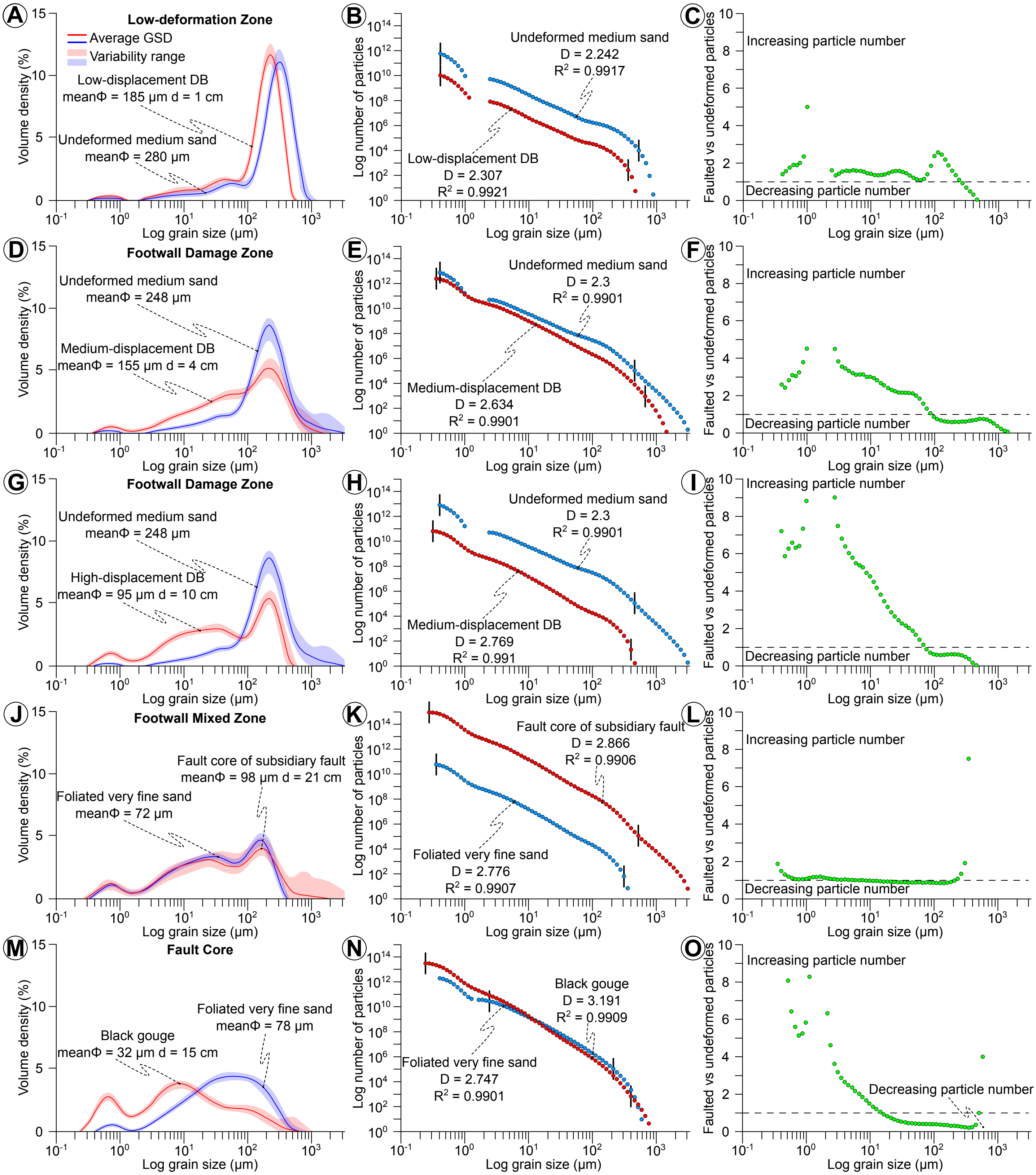
A
Low-deformation Zone
Average GSD
Variability range
Low-displacement DB
meanΦ = 185 μm d = 1 cm
Undeformed medium sand
meanΦ = 280 μm
Volume density (%)
Log grain size (μm)
B
Undeformed medium sand
D = 2.242
R² = 0.9917
Low-displacement DB
D = 2.307
R² = 0.9921
Log number of particles
Log grain size (μm)
C
Increasing particle number
Decreasing particle number
Faulted vs undeformed particles
Log grain size (μm)
D
Footwall Damage Zone
Undeformed medium sand
meanΦ = 248 μm
Medium-displacement DB
meanΦ = 155 μm d = 4 cm
E
Undeformed medium sand
D = 2.3
R² = 0.9901
Medium-displacement DB
D = 2.634
R² = 0.9901
F
Increasing particle number
Decreasing particle number
G
Footwall Damage Zone
Undeformed medium sand
meanΦ = 248 μm
High-displacement DB
meanΦ = 95 μm d = 10 cm
H
Undeformed medium sand
D = 2.3
R² = 0.9901
Medium-displacement DB
D = 2.769
R² = 0.991
I
Increasing particle number
Decreasing particle number
J
Footwall Mixed Zone
Fault core of subsidiary fault
meanΦ = 98 μm d = 21 cm
Foliated very fine sand
meanΦ = 72 μm
K
Fault core of subsidiary fault
D = 2.866
R² = 0.9906
Foliated very fine sand
D = 2.776
R² = 0.9907
L
Increasing particle number
Decreasing particle number
M
Fault Core
Foliated very fine sand
meanΦ = 78 μm
Black gouge
meanΦ = 32 μm d = 15 cm
N
Black gouge
D = 3.191
R² = 0.9909
Foliated very fine sand
D = 2.747
R² = 0.9901
O
Increasing particle number
Decreasing particle number

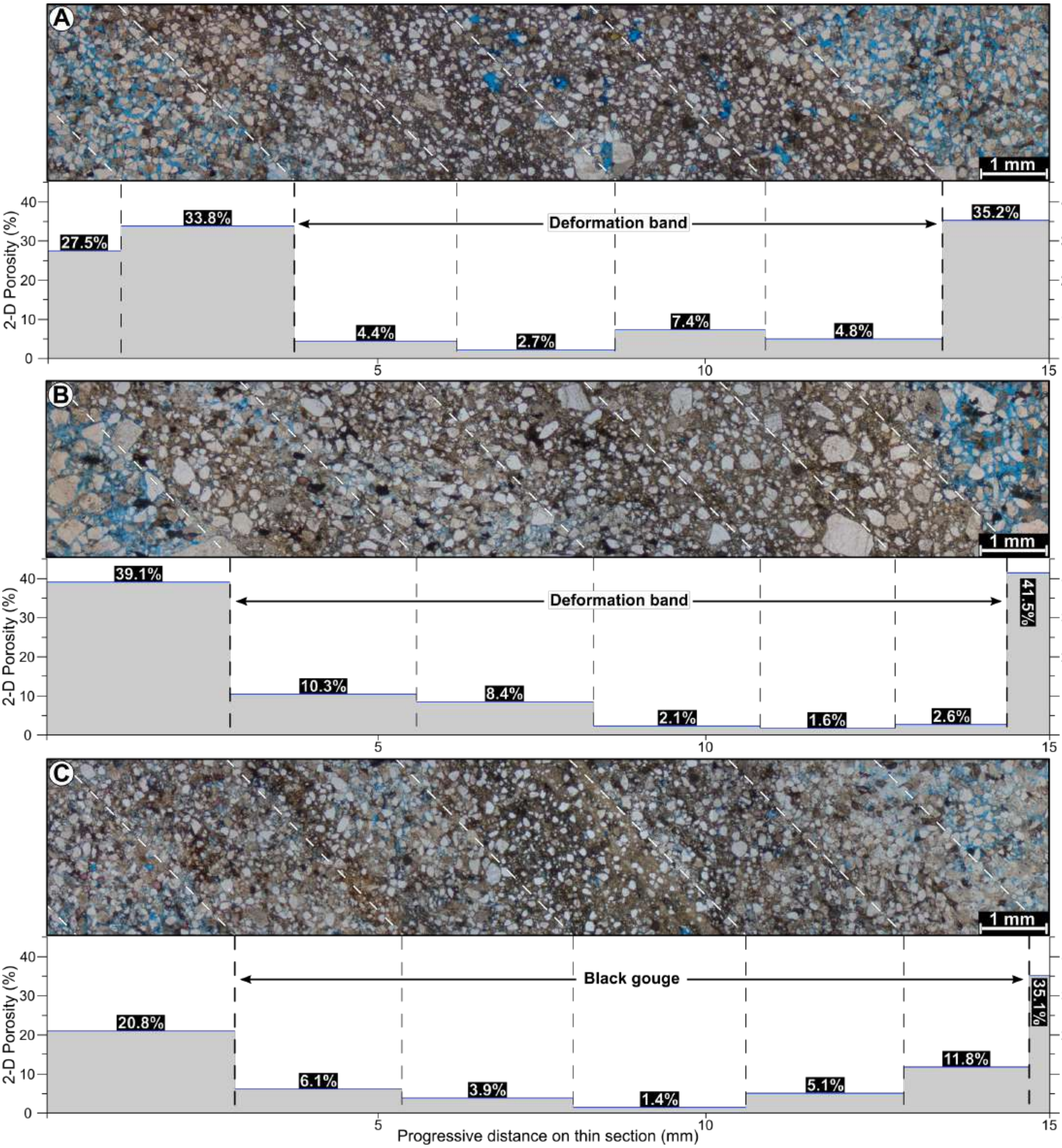

A
1 mm
2-D Porosity (%)
27.5%
33.8%
Deformation band
4.4%
2.7%
7.4%
4.8%
35.2%
B
1 mm
39.1%
Deformation band
10.3%
8.4%
2.1%
1.6%
2.6%
41.5%
C
1 mm
20.8%
Black gouge
6.1%
3.9%
1.4%
5.1%
11.8%
35.1%
Progressive distance on thin section (mm)

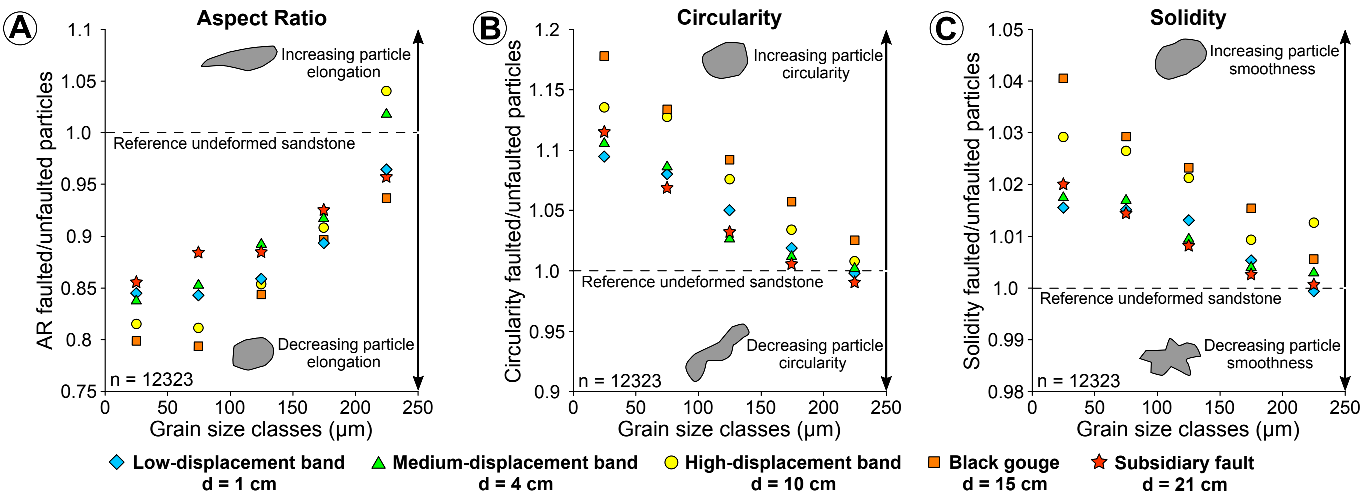
A
Aspect Ratio
AR faulted/unfaulted particles
Increasing particle elongation
Reference undeformed sandstone
Decreasing particle elongation
n = 12323
Grain size classes (μm)
B
Circularity
Circularity faulted/unfaulted particles
Increasing particle circularity
Reference undeformed sandstone
Decreasing particle circularity
n = 12323
Grain size classes (μm)
C
Solidity
Solidity faulted/unfaulted particles
Increasing particle smoothness
Reference undeformed sandstone
Decreasing particle smoothness
n = 12323
Grain size classes (μm)
Low-displacement band d = 1 cm
Medium-displacement band d = 4 cm
High-displacement band d = 10 cm
Black gouge d = 15 cm
Subsidiary fault d = 21 cm

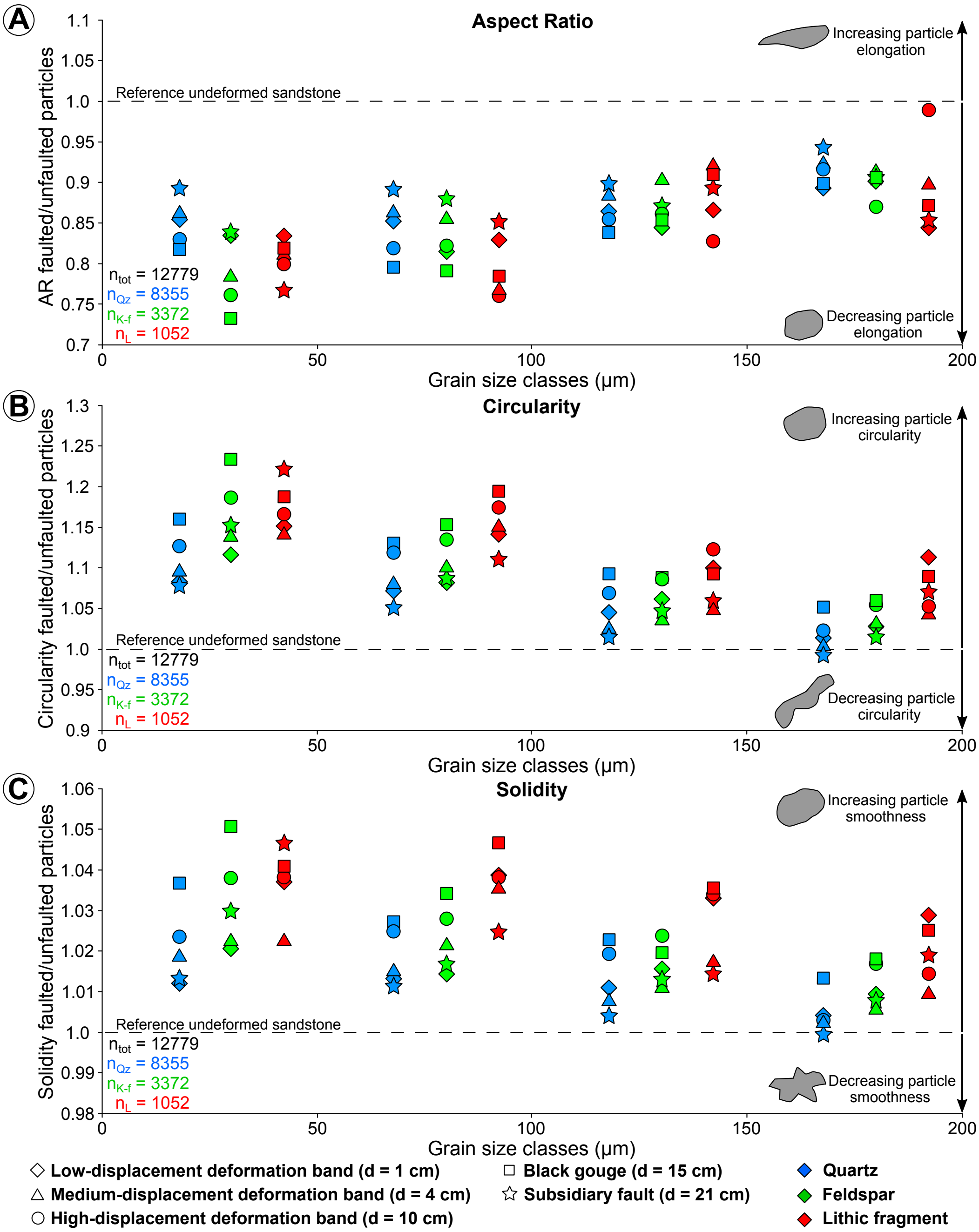

A
Aspect Ratio
AR faulted/unfaulted particles
Reference undeformed sandstone
Increasing particle elongation
Decreasing particle elongation
n_{tot} = 12779
n_{Qz} = 8355
n_{K-f} = 3372
n_L = 1052
Grain size classes (μm)
B
Circularity
Circularity faulted/unfaulted particles
Increasing particle circularity
Decreasing particle circularity
C
Solidity
Solidity faulted/unfaulted particles
Increasing particle smoothness
Decreasing particle smoothness
Low-displacement deformation band (d = 1 cm)
Medium-displacement deformation band (d = 4 cm)
High-displacement deformation band (d = 10 cm)
Black gouge (d = 15 cm)
Subsidiary fault (d = 21 cm)
Quartz
Feldspar
Lithic fragment

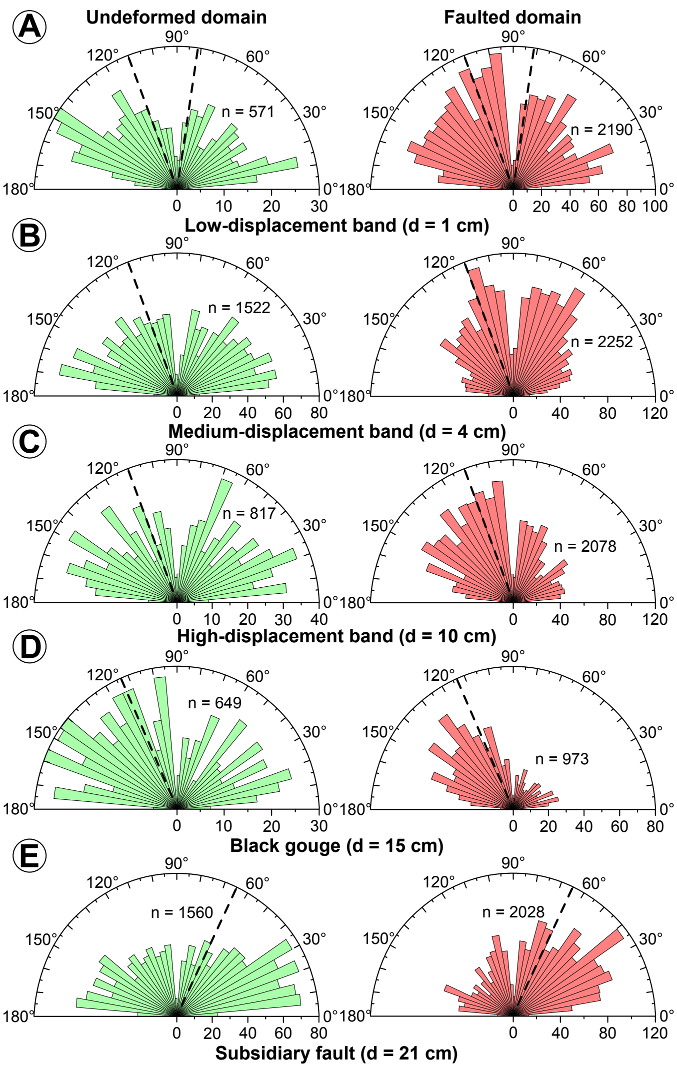
A
Undeformed domain
Faulted domain
n = 571
n = 2190
Low-displacement band (d = 1 cm)
B
n = 1522
n = 2252
Medium-displacement band (d = 4 cm)
C
n = 817
n = 2078
High-displacement band (d = 10 cm)
D
n = 649
n = 973
Black gouge (d = 15 cm)
E
n = 1560
n = 2028
Subsidiary fault (d = 21 cm)
0°
30°
60°
90°
120°
150°
180°

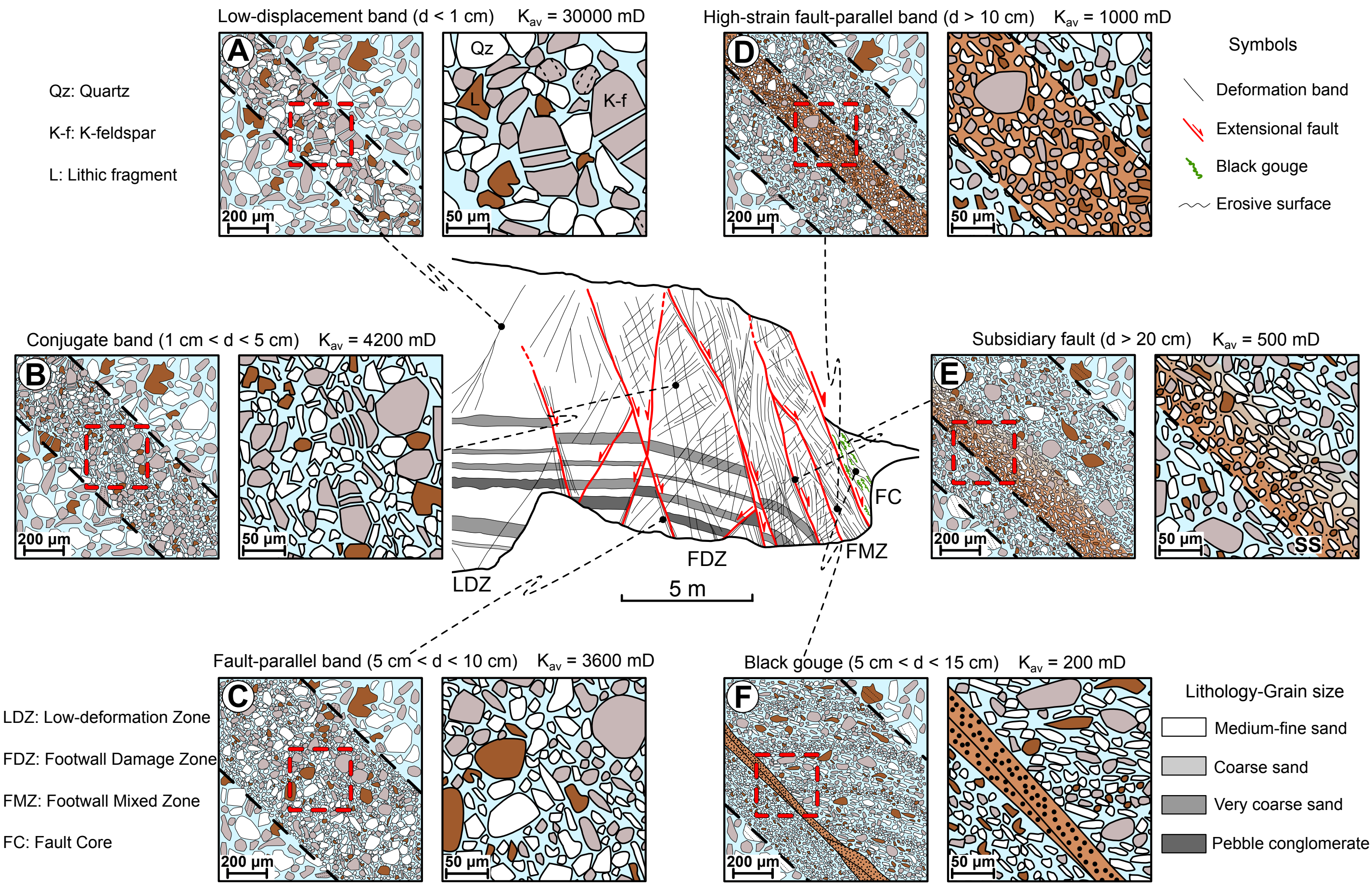

Low-displacement band (d < 1 cm) Kav = 30000 mD
A
Qz
L
K-f
200 µm
50 µm
Qz: Quartz
K-f: K-feldspar
L: Lithic fragment
High-strain fault-parallel band (d > 10 cm) Kav = 1000 mD
D
200 µm
50 µm
Symbols
Deformation band
Extensional fault
Black gouge
Erosive surface
Conjugate band (1 cm < d < 5 cm) Kav = 4200 mD
B
200 µm
50 µm
Subsidiary fault (d > 20 cm) Kav = 500 mD
E
200 µm
50 µm
SS
FC
FMZ
FDZ
LDZ
5 m
Fault-parallel band (5 cm < d < 10 cm) Kav = 3600 mD
C
200 µm
50 µm
LDZ: Low-deformation Zone
FDZ: Footwall Damage Zone
FMZ: Footwall Mixed Zone
FC: Fault Core
Black gouge (5 cm < d < 15 cm) Kav = 200 mD
F
200 µm
50 µm
Lithology-Grain size
Medium-fine sand
Coarse sand
Very coarse sand
Pebble conglomerate

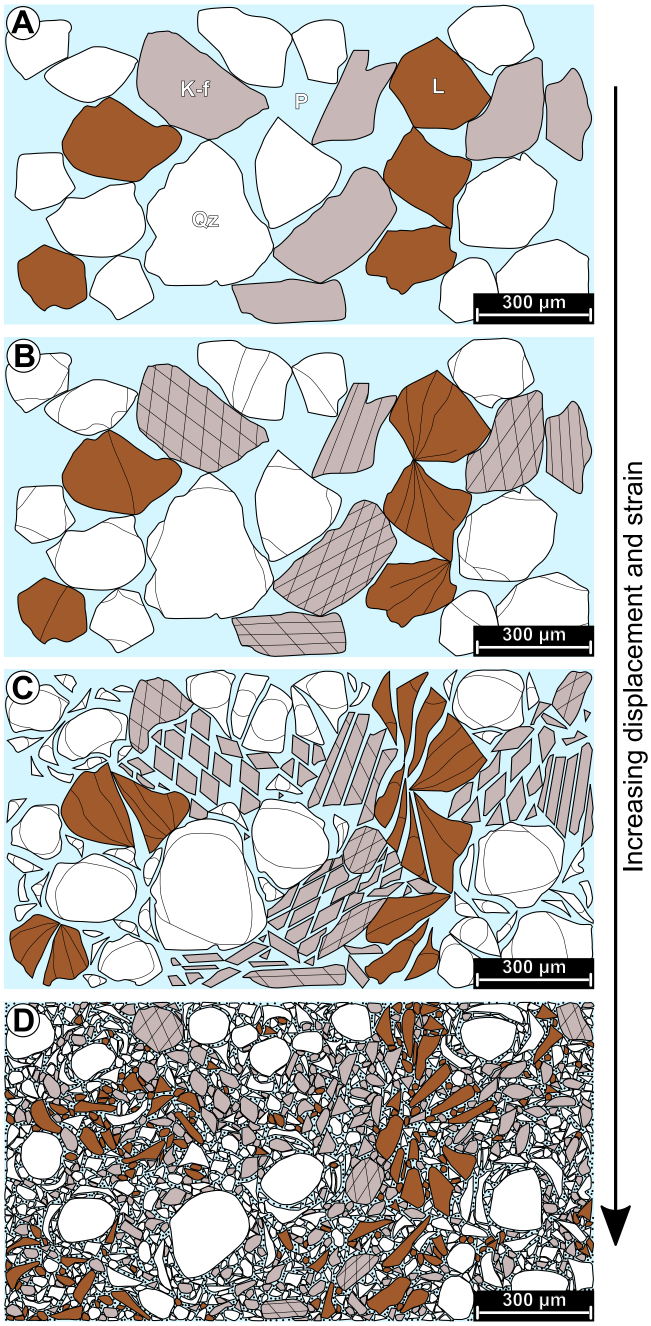
A
K-f
P
L
Qz
300 µm
B
300 µm
C
300 µm
D
300 µm
Increasing displacement and strain

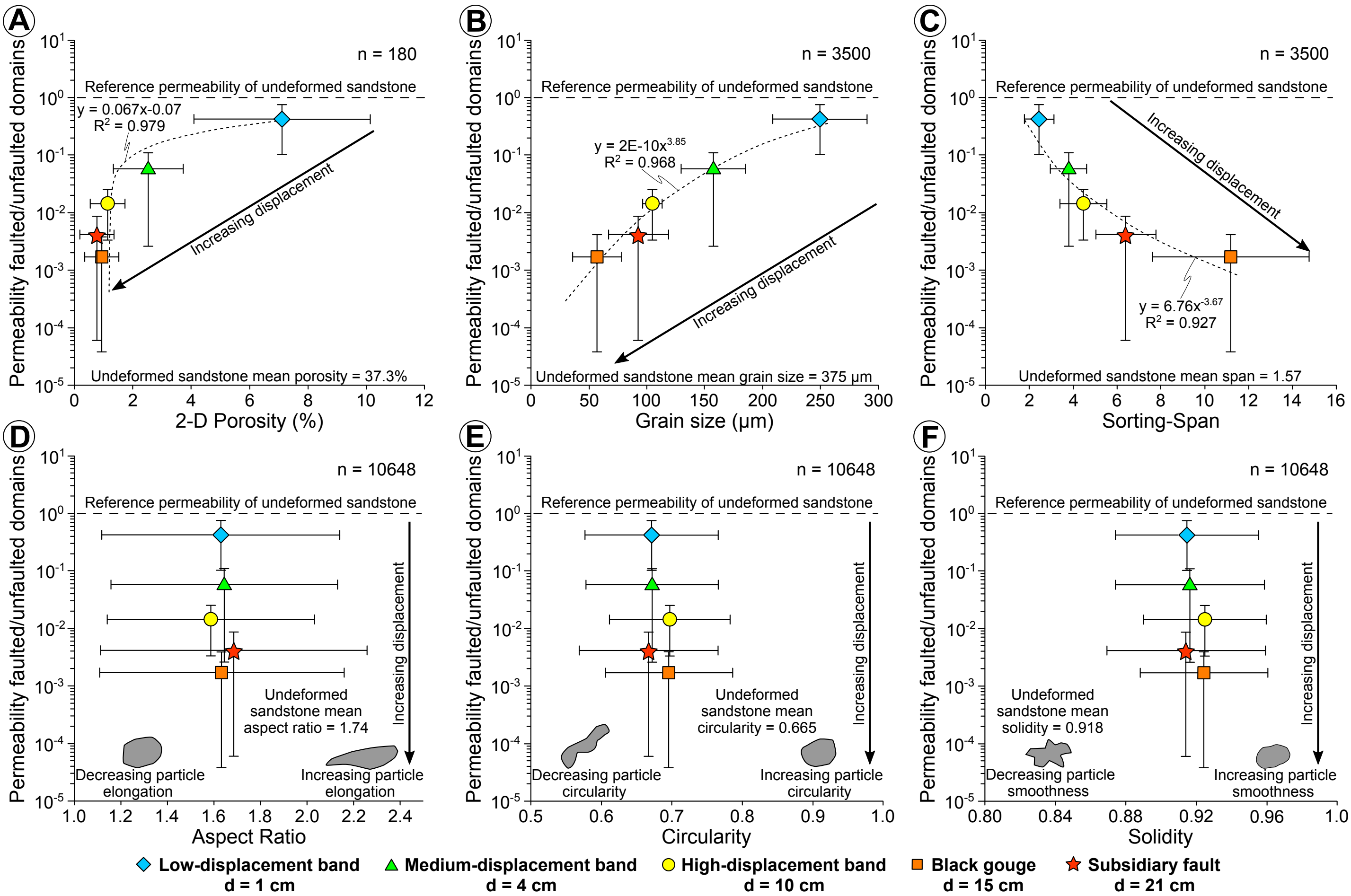
A
n = 180
Reference permeability of undeformed sandstone
y = 0.067x-0.07
R² = 0.979
Increasing displacement
Undeformed sandstone mean porosity = 37.3%
Permeability faulted/unfaulted domains
2-D Porosity (%)
B
n = 3500
y = 2E-10x^3.85
R² = 0.968
Undeformed sandstone mean grain size = 375 μm
Grain size (μm)
C
n = 3500
y = 6.76x^-3.67
R² = 0.927
Undeformed sandstone mean span = 1.57
Sorting-Span
D
n = 10648
Undeformed sandstone mean aspect ratio = 1.74
Decreasing particle elongation
Increasing particle elongation
Aspect Ratio
E
Undeformed sandstone mean circularity = 0.665
Decreasing particle circularity
Increasing particle circularity
Circularity
F
Undeformed sandstone mean solidity = 0.918
Decreasing particle smoothness
Increasing particle smoothness
Solidity
Low-displacement band d = 1 cm
Medium-displacement band d = 4 cm
High-displacement band d = 10 cm
Black gouge d = 15 cm
Subsidiary fault d = 21 cm

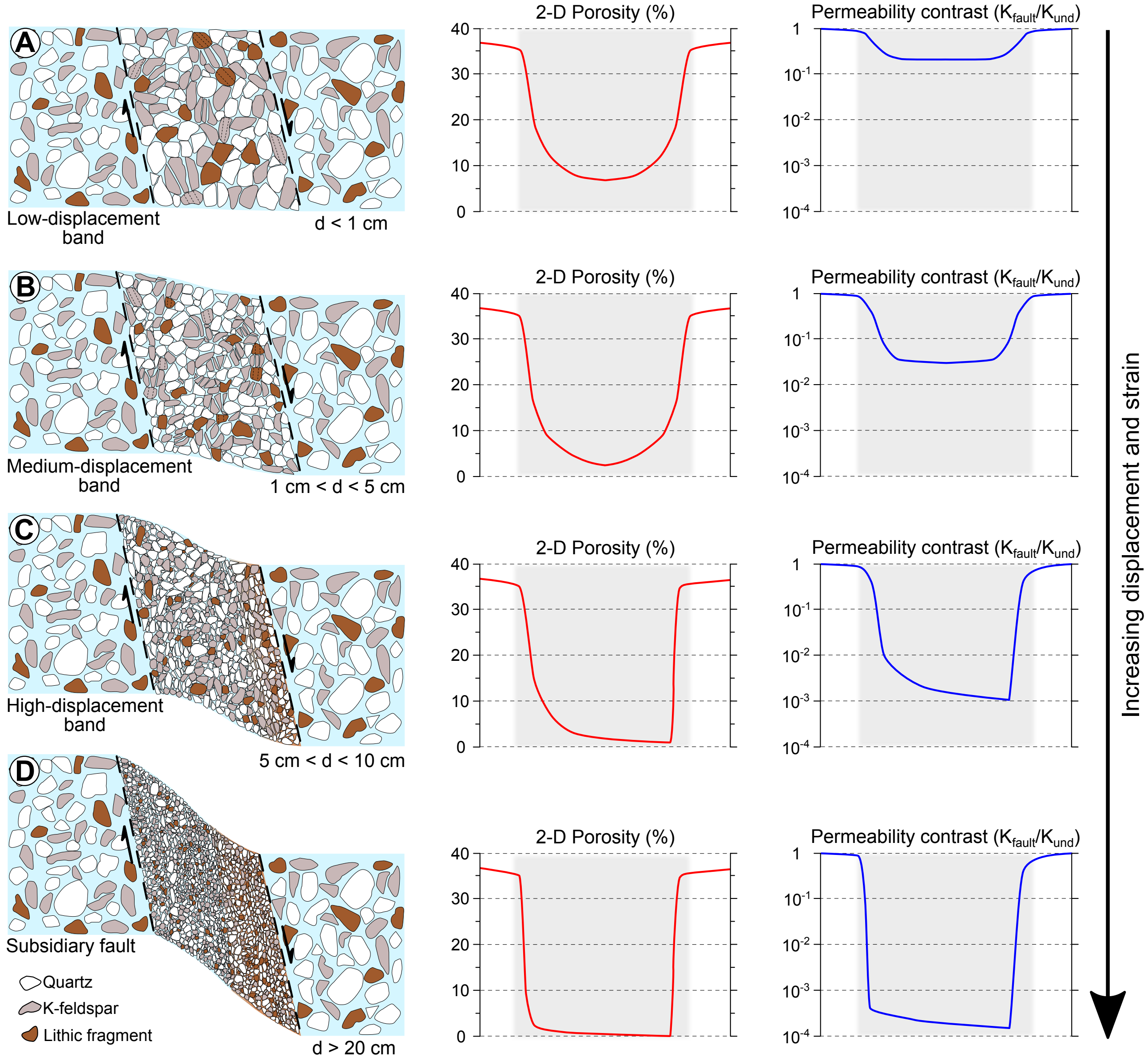

A
Low-displacement band
d < 1 cm
B
Medium-displacement band
1 cm < d < 5 cm
C
High-displacement band
5 cm < d < 10 cm
D
Subsidiary fault
d > 20 cm
Quartz
K-feldspar
Lithic fragment
2-D Porosity (%)
40
30
20
10
0
Permeability contrast (K_{fault}/K_{und})
1
10^{-1}
10^{-2}
10^{-3}
10^{-4}
Increasing displacement and strain